Dynamics of turbulent natural convection in a cubic cavity with centrally placed partially heated inner obstacle

Sofen Kumar Jena, Remi Manceau

Dynamics of Turbulent Natural Convection in a Cubic Cavity with Centrally Placed Partially Heated Inner Obstacle

Sofen Kumar Jena and Rémi Manceau[a)]
Université de Pau et des pays de l'Adour, E2S UPPA, CNRS, Inria, équipe Cagire, LMAP, Pau, France

(*Electronic mail: remi.manceau@univ-pau.fr)

(Dated: 18 July 2024)

Natural convection in a cavity with a partially heated obstacle at the centre at the Rayleigh number $Ra = 1.46 \times 10^9$ is investigated using large-eddy simulation (LES). The standard and dynamic Smagorinsky models, as well as the Wall adapting local eddy-viscosity (WALE) model, are used for the sub-grid scales, and the flow statistics are compared with recent experiments. The LES results obtained with different meshes show overall good agreement with the experiments as concerns the flow and heat transfer. Simulation with a non-ideal wall at the adiabatic side of the obstacle is also performed to explain the residual discrepancies observed in the unheated channel. Additional simulations performed with periodic conditions in the spanwise direction are very different from the full three-dimensional (3D) simulations, which demonstrates the significance of 3D effects in the cavity. In particular, periodic simulations show Tollmien-Schlichting kind waves in the transitional region, while the 3D cavity shows an early cross-flow transition to turbulence.

Keywords: Large-eddy simulation (LES), subgrid-scale model, differentially heated cavity, boundary layer, stratification, internal waves, transition to turbulence, anisotropy, chaos

I. INTRODUCTION

Natural convection in a closed cavity is often encountered in applications, including the cooling of electrical equipment, the design of solar energy collectors, the design of ventilation systems for buildings, and several other household appliances. In addition, natural convection in a cavity with a central obstruction has a wide variety of sophisticated applications, ranging from the cooling of nuclear power plants to the convective motion controlled by the heating of vertical skyscraper walls. In the past, many cubic cavity configurations with a partially/fully heated obstruction have been extensively studied.[1–8] However, the configuration is still advantageous and intriguing for various applications, such as E-enclosures[9] and H-shaped cavities.[10] Applications such as the underhood cooling system of a vehicle are in general in the forced convection regime. However, when the vehicle is stopped with a hot engine, the flow in the underhood compartment is a turbulent natural convection flow in a cavity with a partially heated inner block. Buoyancy is the driving factor for fluid motion and considerably impacts turbulence development in the boundary layers. This configuration has motivated the experimental study of the flow in a cubic cavity with an inner block.[11–14]

Reynolds-averaged Navier–Stokes (RANS) modelling is popular as a powerful and indispensable tool for turbulent simulation at industrial scales, and was frequently applied to cavity flows.[15–21] However, the reliability of RANS computations in natural convection is very sensitive to details of the model, including turbulent length and time scale;[20] as a result, many RANS models estimate flow and heat transfer with insufficient precision. In particular, eddy-viscosity models underestimate the impact of buoyancy on turbulence.[22–28] At sufficiently high Rayleigh number, the flow domain contains multiple regimes with varying characteristics. The upstream boundary layer of the heated obstruction exhibits laminar flow. The downstream travelling waves grow sufficiently and disrupt the vertical laminar boundary layer by ejecting large unsteady eddies.[12] A transitional and fully developed turbulent flow coexists downstream of the heated obstacle wall. These complex features make it difficult for RANS models to accurately reproduce this type of flows.

With the advent of digital computing power in the past few decades, two and three-dimensional transitional and turbulent flows appeared in the literature. Direct numerical simulation (DNS) was used to study the co-existence of laminar, transitional, and fully turbulent regions within buoyant cavities.[29–39] These studies provided information about different scales of motion present in natural convection flows at moderate and high Rayleigh numbers and helped for a physical understanding of turbulence. However, DNS for flow simulation at the engineering scale is not yet feasible. Large eddy simulation (LES) is a promising and viable alternative for the simulation of turbulent natural convection.

The study of natural convection in differentially heated cavities (DHC) using LES was pioneered by Peng and Davidson.[40,41] At low Rayleigh number ($Ra = 1.58 \times 10^9$) the boundary layers are essentially transitional and a model that is too dissipative makes it difficult to predict the transition, and the authors have shown the interest of using a dynamic model for both the subgrid stresses and heat fluxes, and to use a sufficiently fine mesh. These conclusions have motivated many other studies[42–50] investigating the influence of subgrid models in the natural convection regime, in particular to get rid of the use of a constant turbulent Prandtl number. The influence of the model on the transition to turbulence, and in particular the delay caused by an overly dissipative model, has been particularly emphasized by Lau *et al.* [44] and Kizildag *et al.* [47] Another important issue is the consideration of sufficiently real-

[a)]https://team.inria.fr/rmanceau/en/

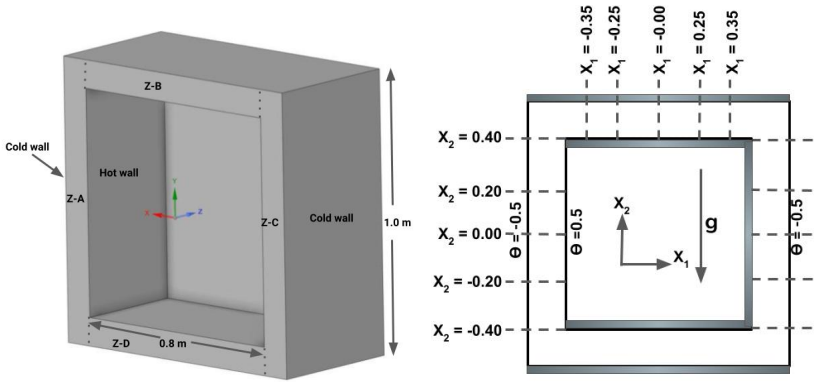

(a) (b)

FIG. 1: Schematic diagram of the numerical setup used for analysis (a) 3D representation across the symmetry plane in the spanwise direction (b) 2D view of the setup (dotted lines show the measurement planes)

istic boundary conditions to reproduce the experimental conditions, whether it concerns the influence of 3D effects[44,51] or of thermal boundary conditions at the walls.[52,53]

These conclusions from the literature must be kept in mind when considering the more complex configuration of an enclosure having a partially heated centrally placed obstacle (Fig. 1), experimentally studied by Weppe, Moreau, and Saury.[12] This configuration is a geometrically simple but physically relevant representation of the underhood space of automobiles. One wall of the centrally placed block, which plays the role of the engine, is heated to an imposed temperature while the remaining sides are insulated. The top, bottom, front and back walls of the cavity are adiabatic, and the other walls are at an imposed cold temperature. The Rayleigh number is $Ra = 1.46\times10^9$, based on the height of the inner block, and the Prandtl number is $Pr = 0.71$. The whole geometry can be divided into four zones, as shown in Fig. 1a. Zone A is a differentially heated vertical channel, and the natural convection flow initiated in this zone generates a flow in the whole cavity. The results are compared with the experimental database of Weppe, Moreau, and Saury [12] to depict the behaviour of the turbulence model to reveal the associated dynamics with the onset of natural convection in the system.

II. PRESENTATION OF THE METHODOLOGY

A. Governing Equations

This study focuses on the natural convection of air in the annular 3D cavity submitted to a horizontal thermal gradient in Zone A, shown in Figure 1. LES equations are obtained by applying a low-pass filtering operation to any flow field variable $\phi(\mathbf{x},t)$ in the flow domain Ω, expressed as

$$\overline{\phi}(\mathbf{x},t) = \int_\Omega \phi(\mathbf{x}',t)G(\mathbf{x},\mathbf{x}')\,\mathrm{d}\mathbf{x}'. \tag{1}$$

G is the filter kernel, parametrized by a filter width Δ. The instantaneous field variable ϕ is expressed as

$$\phi = \overline{\phi} + \phi_{SGS}. \tag{2}$$

$\overline{\phi}$ represents the filtered, or resolved part of the variable, and ϕ_{SGS} is the unresolved or subgrid-scale (SGS) component. Within our unstructured finite-volume framework, the filter width is the cube root of the cell volume.

The flow is characterized by two dimensionless numbers: the Rayleigh number

$$Ra = \frac{g\beta H_b^3(T_H - T_C)}{\nu\alpha} = 1.46\times10^9, \tag{3}$$

and the Prandtl number

$$Pr = \frac{\mu C_p}{\lambda} = 0.71. \tag{4}$$

$H_b = 0.8m$ is the size of the cubic heated block, and T_H and T_C the hot and cold temperatures imposed at the walls as shown in Fig. 1a. The properties of the fluid at the reference temperature $T_r = (T_H + T_C)/2$ are the density ρ_r, the kinematic viscosity ν, the thermal conductivity λ, the specific heat C_p and the thermal diffusivity $\alpha = \lambda/(\rho_r C_p)$, and g is the acceleration due to gravity. The primitive flow field variables are non-dimensionalized as follows: $x_i = \dfrac{\widehat{x}_i}{L}$, $t = \dfrac{\widehat{t}\,\alpha}{LH_b}Ra^{0.5}$, $u_i = \dfrac{\widehat{u}_i H_b}{\alpha}Ra^{-0.5}$ and $\Theta = \dfrac{\widehat{T}-T_r}{T_H - T_C}$. $L = 1m$ is the length of the cubic cavity. $\widehat{x}_i$ are the cartesian coordinates, $\widehat{t}$ the physical time, $\widehat{u}_i$ the components of velocity and $\widehat{T}$ the temperature. As the experiment was designed to ensure that density variations are sufficiently moderate for the Boussinesq approximation to be valid,[13] the latter is used and the density in the buoyancy term is related to the temperature as

$$\rho = \rho_r\left[1 - \beta(T - T_r)\right], \tag{5}$$

where β is the thermal expansion coefficient. With the Boussinesq approximation, the filtered continuity equation is expressed as

$$\frac{\partial \overline{u}_i}{\partial x_i} = 0 \tag{6}$$

and the filtered momentum equations as

$$\frac{\partial \overline{u}_i}{\partial t} + \overline{u}_j \frac{\partial \overline{u}_i}{\partial x_j} = -\frac{\partial \overline{p}}{\partial x_i} + \left(\frac{H_b}{L}\right) PrRa^{-0.5} \frac{\partial^2 \overline{u}_i}{\partial x_j \partial x_j} + \left(\frac{L}{H_b}\right) Pr\overline{\Theta}\delta_{ik} - \frac{\partial \tau_{ij}}{\partial x_j}. \tag{7}$$

The term $\tau_{ij} = \overline{u_i u_j} - \overline{u}_i \overline{u}_j$ in the right hand side of Equation (7) represents the SGS stresses. Neglecting the radiative heat transfer and viscous heating, the energy equation is expressed as

$$\frac{\partial \overline{\Theta}}{\partial t} + \overline{u}_j \frac{\partial \overline{\Theta}}{\partial x_j} = \left(\frac{H_b}{L}\right) Ra^{-0.5} \frac{\partial^2 \overline{\Theta}}{\partial x_j \partial x_j} - \frac{\partial h_j}{\partial x_j}, \tag{8}$$

where $h_j = \overline{u_i \Theta} - \overline{u}_i \overline{\Theta}$ is the SGS heat flux.

B. Subgrid-scale models

The governing equations (7)-(8) are unclosed, and require modelling of the SGS stress τ_{ij} and heat flux h_j. The filtered rate-of-strain tensor is expressed as

$$\overline{S}_{ij} = \frac{1}{2}\left(\frac{\partial \overline{u}_i}{\partial x_j} + \frac{\partial \overline{u}_j}{\partial x_i}\right) \tag{9}$$

The SGS models used herein are based on the subgrid viscosity hypothesis

$$\tau_{ij} - \frac{1}{3}\tau_{kk}\delta_{ij} = -2\nu_{SGS}\overline{S}_{ij}. \tag{10}$$

The SGS heat flux h_j is modelled using simple gradient diffusion hypothesis (SGDH)

$$h_j = -\frac{\nu_{SGS}}{Pr_{SGS}} \frac{\partial \overline{\Theta}}{\partial x_j}, \tag{11}$$

where Pr_{SGS} is the SGS Prandtl number.

The following three SGS models are used in the present study

1. The Smagorinsky-Lilly model[54,55] with Van Driest's[56] damping function for correction near the wall;
2. The dynamics Smagorinsky model of Germano *et al.*;[57]
3. The Wall-Adapting Local Eddy-viscosity (WALE) model of Nicoud and Ducros.[58]

LES are carried out using the open-source solver code_saturne, developed by EDF. The flow is resolved up to the wall using wall-adjacent cells with $y^+ < 0.4$, $x^+ < 4$ and $z^+ < 4$. The SIMPLEC algorithm is employed for pressure velocity coupling. A least square method is used for the gradient reconstruction. Central difference discretization scheme is used with a slope limiter.

C. Reference experiment

The experimental setup of Weppe, Moreau, and Saury [12] consists of a partially side-heated cubic obstacle of length $H_b = 0.8m$ positioned in the center of a cubic cavity of inner dimension $1m$ (Figure 1a) with a distance of $0.1m$ between the inner obstacle and the surrounding cavity. The vertical walls of the cavity are made of aluminium ($\lambda = 174\,W\,m^{-1}\,K^{-1}$ and $\varepsilon = 0.10$), and two heat exchangers maintain isothermal boundary conditions. The top and bottom adiabatic walls of the cavity are made of $100mm$ thick extruded polystyrene ($\lambda = 0.035W\,m^{-1}\,K^{-1}$) covered with low emissivity Mylar sheets ($\varepsilon = 0.08$) to minimize the radiation effects. Glass panels are used in the front and rear walls of the cavity for flow visualization with insulated polystyrene layers. The centrally placed obstacle is made of $40mm$ thick aluminium plates ($\lambda = 174W\,m^{-1}\,K^{-1}$ and $\varepsilon = 0.10$), and a heating wire heats one wall of the obstacle. The top, bottom, front, and rear walls of the obstacle are covered with $4mm$ POM-C plates and low-emissivity Mylar sheets ($\varepsilon = 0.08$). The obstacle is filled with a succesions of Rockwool panels along with etalon to prevent heat transfer from the heated wall to the other sides of the obstacle. Experimental temperatures are monitored using K-type thermocouples and sampled at $60hz$ frequency using a 34972A data acquisition unit. Particle Image Velocimetry (PIV) is used for velocity measurements. A pulsed Nd:YAG laser is used to generate the laser sheet ($2 \times 50mJ@100Hz$). Paraffine oil particle tracers having diameter $d = 5\mu m$ are generated by the smoke generator. These particles are visualized with a CMOS camera with 2560×2160 pixels. The pixel pitch size is $7\mu m$, and the field size is $120 \times 105mm$. Five thousand pairs of images are acquired at $25Hz$, and the time between two frames is in the range $1000 - 8000\mu s$. Image processing is done through the LaVision PIV algorithm to obtain velocity vectors. Measurements are performed in the three zones called Zones A, B and C, shown in Figure 1a, and the flow statistics are extracted along the profiles located in the mid-plane as shown in Figure 1b. Further information is available in Weppe, Moreau, and Saury.[12]

III. RESULTS AND DISCUSSION

A. Geometric Details & Effect of Mesh on Flow Statistics

Two geometric configurations, a fully realistic cavity (FRC) and a periodic approximated cavity (PAC), are considered for the present LES simulation. The configuration is symmetric in the spanwise (x_3) direction; hence only half of the geometry is taken for FRC with a symmetric boundary condition in the $x_3 = 0$ plane. This FRC accounts for the end wall boundary conditions in the spanwise direction. In a periodic approximated cavity (PAC), a finite thickness slice of the annular configuration in $x_1 - x_2$ plane is considered with periodic boundary conditions in the spanwise direction. Therefore, PAC ignores both thermal and hydrodynamic boundary conditions at $x_3 = \pm 0.5$. The PAC configuration is used here to study the significance of 3D effects in this flow, which could not be confirmed by the experimental study of Weppe, Moreau, and Saury.[12]

Two different types and three different mesh refinements are used for the computation of FRC. Figures 2a & 2c show

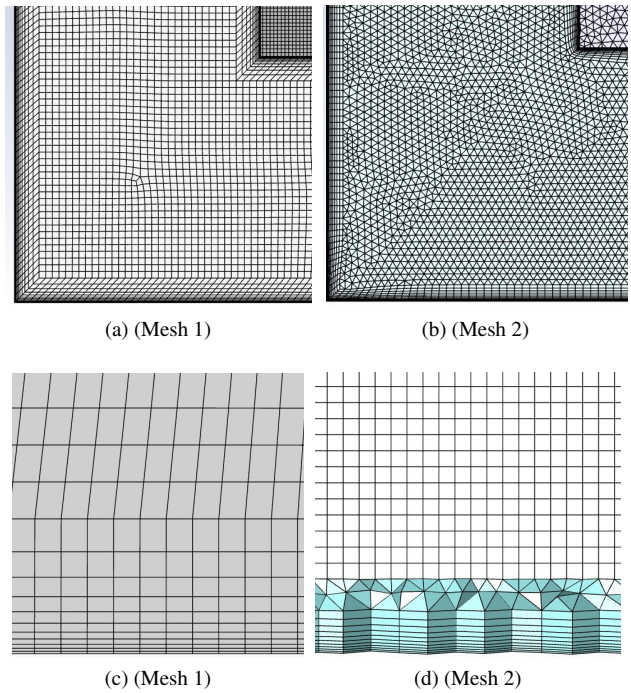

(a) (Mesh 1) (b) (Mesh 2)

(c) (Mesh 1) (d) (Mesh 2)

FIG. 2: (a) and (c), Mesh 1: Fully hexagonal mesh with quad elements at the surface, (b) and (d), Mesh 2: Hexagonal core with tet elements at the surface. For both meshes, cell count is around 24 million. (a) and (b), view of the lower left corner. (c) and (d), zoom on the near-wall region.

Mesh 1, which has a fully hexagonal core mesh having tetragonal surface elements. Figures 2b & 2d show Mesh 2, which has a hexagonal core with triangular surface elements and smooth wall prism layer transition near the solid wall to resolve the steep gradients. Mesh 1 with three different cell counts (16 million, 24 million and 34 million) is tested. Mesh 2, with a 24 million cell count, is also tested to compare the effect of mesh type on the flow statistics. LES are performed with the WALE model for all kinds of mesh discussed above, and the results obtained in the differentially heated cavity (Zone A) are shown in Figure 3. Mesh 1, having 16 million elements, shows good agreement with other meshs and experimental results in the lower part of the cavity (Figure 3g). However, the same mesh failed significantly in the upper part of the cavity (Figures 3a, 3c and 3e). A bare minimum flow statistics deviation is noticed from Mesh 1 type to Mesh 2 type, having a 24 million cell count. In the rest of the paper, the FRC computations are performed using Mesh 1 with 34 million cell elements. Beside this FRC case, three different PACs are considered, with slice thicknesses of $\Delta x_3 = 0.05$, $\Delta x_3 = 0.1$ and $\Delta x_3 = 0.2$, and mesh-independent first-order statistics for each PAC are obtained with about 9.5 million hexagonal mesh.

B. Overall Dynamical Behavior of the Flow in the Cavity

Figure 4 represents the streamlines in the $x_1 - x_2$ plane at $x_3 = 0$, for the WALE model. The mean flow in the cavity is characterised by forming a vertical thin boundary layer along the hot wall of the obstacle and a thick core region in Zone A. A counterclockwise rotating loop is formed in Zone A from $x_2 = -0.4$ to $x_2 = 0.5$ with multiple regionally formed rotating vortices. The disturbances in the boundary layer are amplified due to the formation of these vortices[30,59] and the boundary layer eventually becomes turbulent. Because of the intense upward turbulent motion, secondary vorticity is formed between $x_2 = 0.4$ to $x_2 = 0.5$ in Zone A. Above the corner of the inner obstacle, a turbulent mixing layer forms, which impacts on the top of the cavity and generates the rotating region in the upper part of Zone A and the flow in Zone B. Multiple rotating structures are formed in the horizontal channel in Zone B due to interactions with Zones A and C. Motion in Zone C is dominated by the downward boundary layer along the cold wall at $x_1 = 0.5$ and rotating vorticity at the exit of Zone B. The flow relaminarises in Zone C as it progresses along the cold isothermal wall. The flow remains laminar in Zone D, and a streamlined flow field is formed with a rotating loop downstream due to coupling with the rotating plumes in Zone A.

C. Comparison of LES and experiments in FRC

Figures 5, 7 and 8 show the mean velocity and temperature profiles in Zone A, B and C, respectively. Before delving into the details of boundary layer development and general flow circulation in the cavity, it is worth focusing on the aspect that first comes to mind in these figures, which is that the three LES models give virtually identical results. This is because the mesh is fine enough for the simulations to be nearly DNS, and the influence of the LES model is very small. This can be seen by looking at the LES indicator of quality (LESIQ) in-

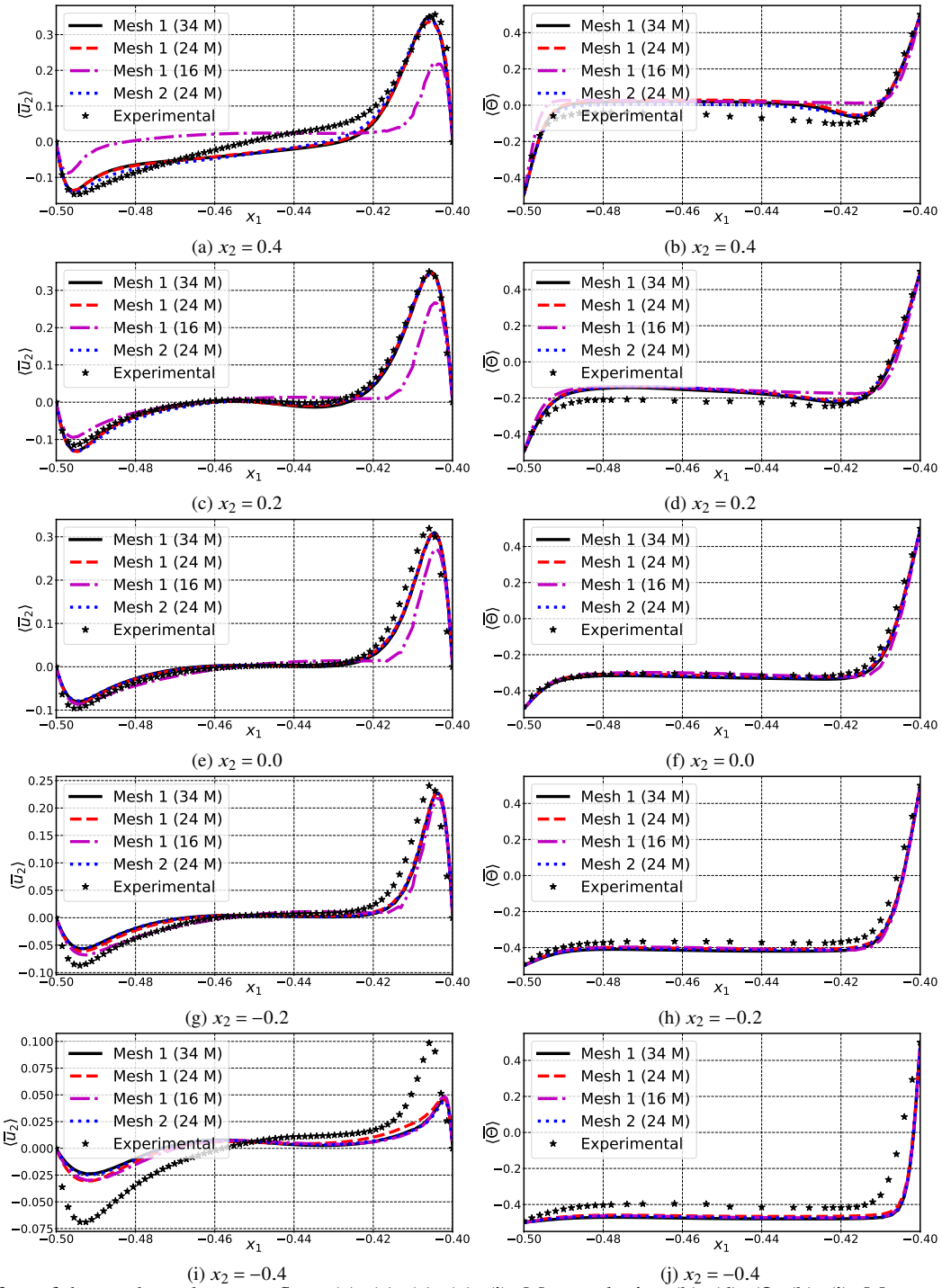

(a) $x_2 = 0.4$ (b) $x_2 = 0.4$

(c) $x_2 = 0.2$ (d) $x_2 = 0.2$

(e) $x_2 = 0.0$ (f) $x_2 = 0.0$

(g) $x_2 = -0.2$ (h) $x_2 = -0.2$

(i) $x_2 = -0.4$ (j) $x_2 = -0.4$

FIG. 3: Effect of the mesh on the mean flow. (a), (c), (e), (g), (i): Mean velocity. (b), (d), (f), (h), (j): Mean temperature.

troduced by Celik, Cehreli, and Yavuz [60] as a quality measure criterion for LES,

$$\mathrm{LESIQ} = \frac{1}{1+0.05\left(\frac{\nu+<\nu_t>}{\nu}\right)^{0.53}}, \qquad (12)$$

where ν and ν_t are laminar and subgrid-scale kinematic viscosity, respectively, and $<.>$ stands for the long-time average. LESIQ is a dimensionless number between zero and one. LESIQ > 0.8 is the indicator of good LES while LESIQ ≥ 0.95 is considered as DNS.[61] The fact that LESIQ ≈ 0.95 for the present LES (Figure 6) shows that the mesh is sufficiently fine for the influence of the LES model to be very small, and average statistics of flow quantities are virtually indistinguishable.

Figure 5 represents the mean vertical velocity $<\overline{u}_2>$ and

(a) (b)

FIG. 4: Streamlines at $x_3 = 0$. (a) FRC, (b) PAC.

temperature $<\overline{\Theta}>$ profiles in Zone A at $x_3 = 0$ for different SGS models. The abbreviation NIW stands for non-ideal wall, a case which is briefly covered below. The flow along the hot wall becomes increasingly turbulent with intense mixing, which results in stratification of the mean temperature field (Figures 5b, 5d, 5f, 5h & 5j). The mean vertical velocity profiles show peaks adjacent to the hot and cold walls, with mean velocity falling to zero in the middle of the channel. For $x_2 \geq 0$, all SGS models predict a rather good matching in the dynamic boundary layers with the experimental results (Figures 5a, 5c & 5e). The peak velocity in the boundary layer along the hot wall is up to three times larger than the one along the cold wall. A part of the descending flow along the cold wall at $x_2 = -0.4$ fuels the flow along the hot wall, and another part tries to penetrate the lower horizontal channel in Zone D, and mix with the incoming horizontal streamlined jet in the channel, resulting in a recirculating loop at the trailing end of Zone D (Figures 4). A part of the incoming horizontal flow in the lower channel feeds the vertical developing hot boundary layer. Temperature profiles at different elevations in Figure 5 show the formation of thermal boundary layers at the hot and cold walls. The temperature in the central part of the channel increases along the vertical direction. However, all models overpredict the temperature compared to the experiment in the upper part of the channel (Figures 5b & 5d). For $x_2 < 0$, the simulated temperature field is under-predicted compared to the experiment (Figures 5h & 5j).

It is noted the velocity and temperature fields appear to have a mismatch: velocity is best predicted at $x_2 = 0.2$, while temperature corresponds better overall to experimental data at $x_2 = 0$. However, a distinction must be made between what happens in the ascending boundary layer and in the core of the flow. The boundary layer is very well reproduced from $x_2 = 0.2$, for both velocity and temperature fields. However, the stratification in the core of the flow is too strong, such that temperature is overestimated at $x_2 = 0.2$. This stratification is linked to the temperature field in the whole cavity, and is therefore independent of the local velocity, which is in fact zero. This explains the decoupling of the velocity and temperature fields mentioned above.

At $x_2 = -0.4$, the computed velocity field is highly underpredicted compared to the experiment (Figures 5i). This mismatch is possibly due to non-ideal experimental conditions, which can have a profound effect on natural convection. In the experiment, it was challenging to create a perfectly insulated barrier. Barhaghi and Davidson [59] also discussed the limitations of the adiabatic boundary condition assumption for recreating experimental results from simulation since they are notoriously difficult to achieve in practice. It is especially visible in figures 7 and 8 the presence of a heat flux at the walls of the internal obstacle, while, in simulation, the temperature gradient is zero at the wall. It can be seen at the bottom of zone C (Figure 8j) that due to this residual heating at all the walls of the internal obstacle, the temperature is higher in the experiments than in the simulations, such that, the flow enters Zone A with a relatively high temperature in the experiment compared to the simulation (Figure 5j). Due to the induced buoyant force, the experimental velocity at $x_2 = -0.4$ is relatively high (Figure 5i). All SGS models fail to predict velocity at this location, as they are performed using adiabatic conditions. This initial discrepancy at the bottom of the ascending boundary layer along the hot wall has a significant impact up to $x_2 = 0.2$ (Figure 5c), where the initial condition is finally forgotten. Identical reproduction of the experimental results would require information on exact heat losses across the walls.

The flow leaving from the trailing end of the heated face of the obstacle enters into Zone B. The horizontal mean velocity profiles at $x_1 = -0.35$ show an horizontal wall jet along the upper wall of the cavity (Figures 7a). This wall jet thickens until the middle of the channel $x_1 = 0$ and looses strength. A very low horizontal velocity persists in the upper face of the obstacle $x_1 = 0$ to $x_1 = 0.35$. The clockwise rotating structure in the trailing end of the Zone B produces a symmetric bending of the horizontal mean velocity at $x_1 = 0.25$ and $x_1 = 0.35$ (Figures 7d & 7e). LES temperature profiles are flat in Zone

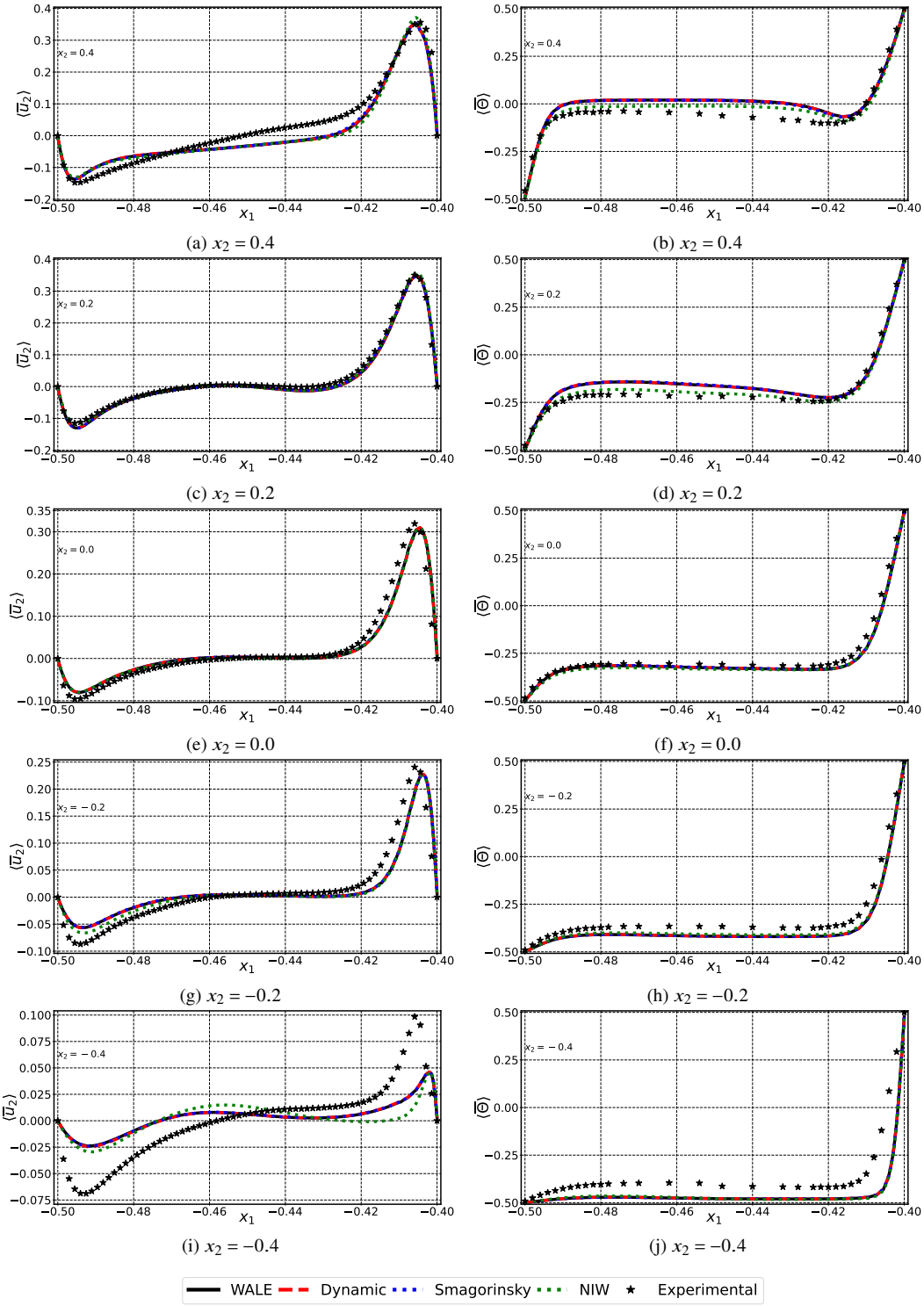

FIG. 5: Horizontal profiles in Zone A. (a), (c), (e), (g), (i): Mean velocity. (b), (d), (f), (h), (j): Mean temperature.

B. The experimental measurements on the cavity Zone B have revealed temperature distributions in clear disagreement with the numerical results in the vicinity of the adiabatic top wall of the obstacle (Figures 7f-7j). A temperature gradient in the vicinity of the nominally adiabatic wall for experimental measurements is the footprint of the heat losses. In the proximity of the heated wall, conduction in the aluminium plate mounted on the obstacle left (heated) face is responsible for the strong temperature gradient (Figure 7f). A similar observation can be made on the trailing end of the channel, where heat leaks into

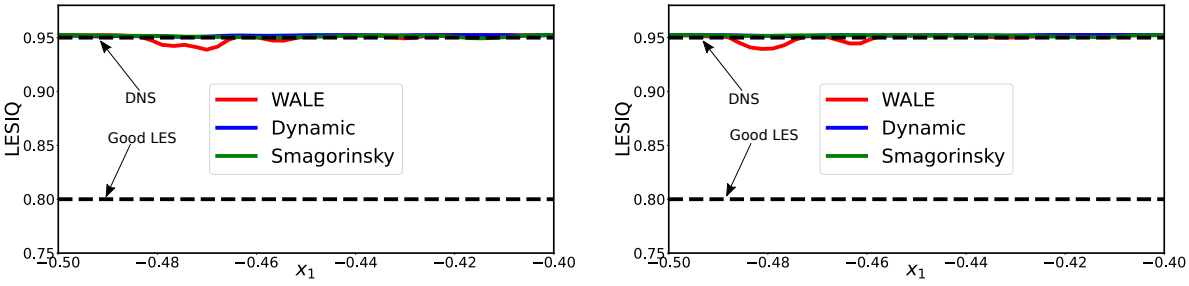

FIG. 6: LESIQ for different subgrid-scale models at $x_3 = 0$. (a) $x_2 = 0.4$, (b) $x_2 = 0.2$.

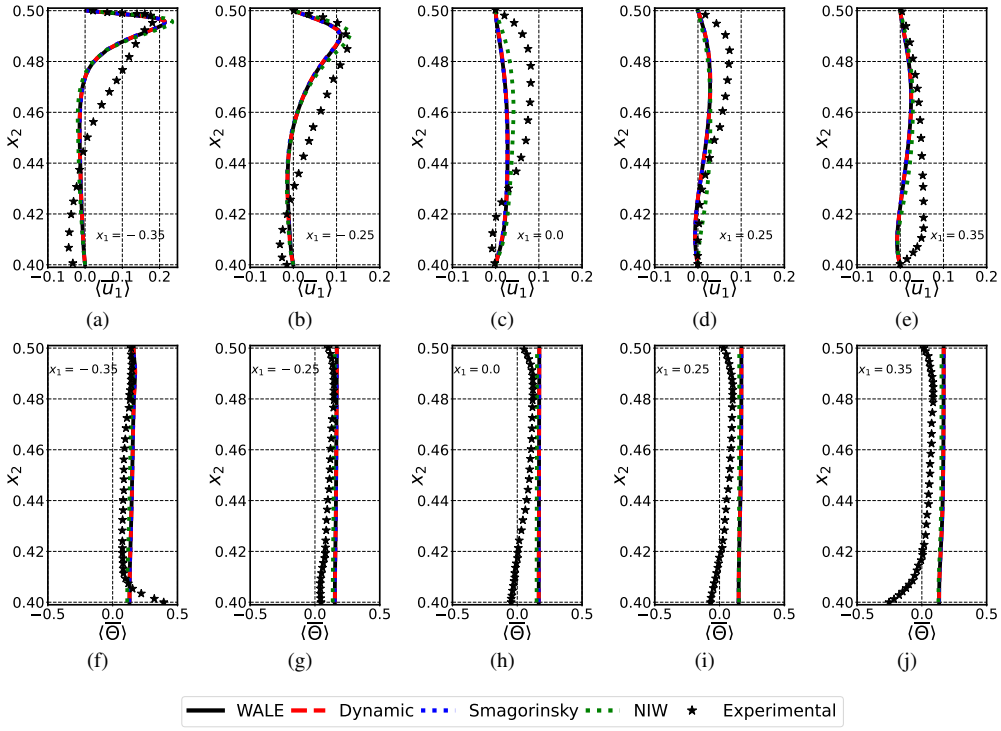

FIG. 7: Vertical profiles in Zone B. (a), (b), (c), (d), (e): Mean velocity. (f), (g), (h), (i), (j): Mean temperature.

the aluminium plate used at the right side of the obstacle for providing structural strength. The numerical temperature distribution is almost uniform between the two adiabatic walls, which shows the accounting for the non-ideal adiabatic walls is missing in the LES performed.

The flow then enters Zone C (Figure 8). A downward vertical boundary layer is formed along the cold wall. This boundary layer has a quite similar trend as the cold boundary layer of Zone A. The growth of the thermal boundary layer is visible along the cold wall (Figures 8b, 8d, 8f, 8h & 8j). Large discrepancies are observed along the nominally adiabatic wall. Under ideal conditions, all SGS models predict zero average vertical velocity due to the absence of temperature difference between the wall and the core of the flow. In contrast, a flow is generated in the experiment, due to the presence of an aluminum plate on this face of the cubic obstacle, used to rigidify the experimental setup. The conduction in this plate induces a uniformization of the temperature on this face. It can be seen in Figure 8 that the simulations give a temperature at the wall located at $x_1 = 0.40$ that decreases from almost 0.1 at the top to almost -0.5 at the bottom, while the experiments show a temperature which remains close to -0.3 everywhere. The wall temperature cooler than the core of the flow generates a descending boundary layer along the upper part of this wall. Below $x_2 = 0.2$, the core of the flow has cooled due to the presence of the cold wall at $x_1 = 0.5$, generating an ascending boundary layer. In order to understand how much this thermal boundary condition influences the whole flow in the cavity, a case with a non-ideal wall (NIW) is investigated, where the

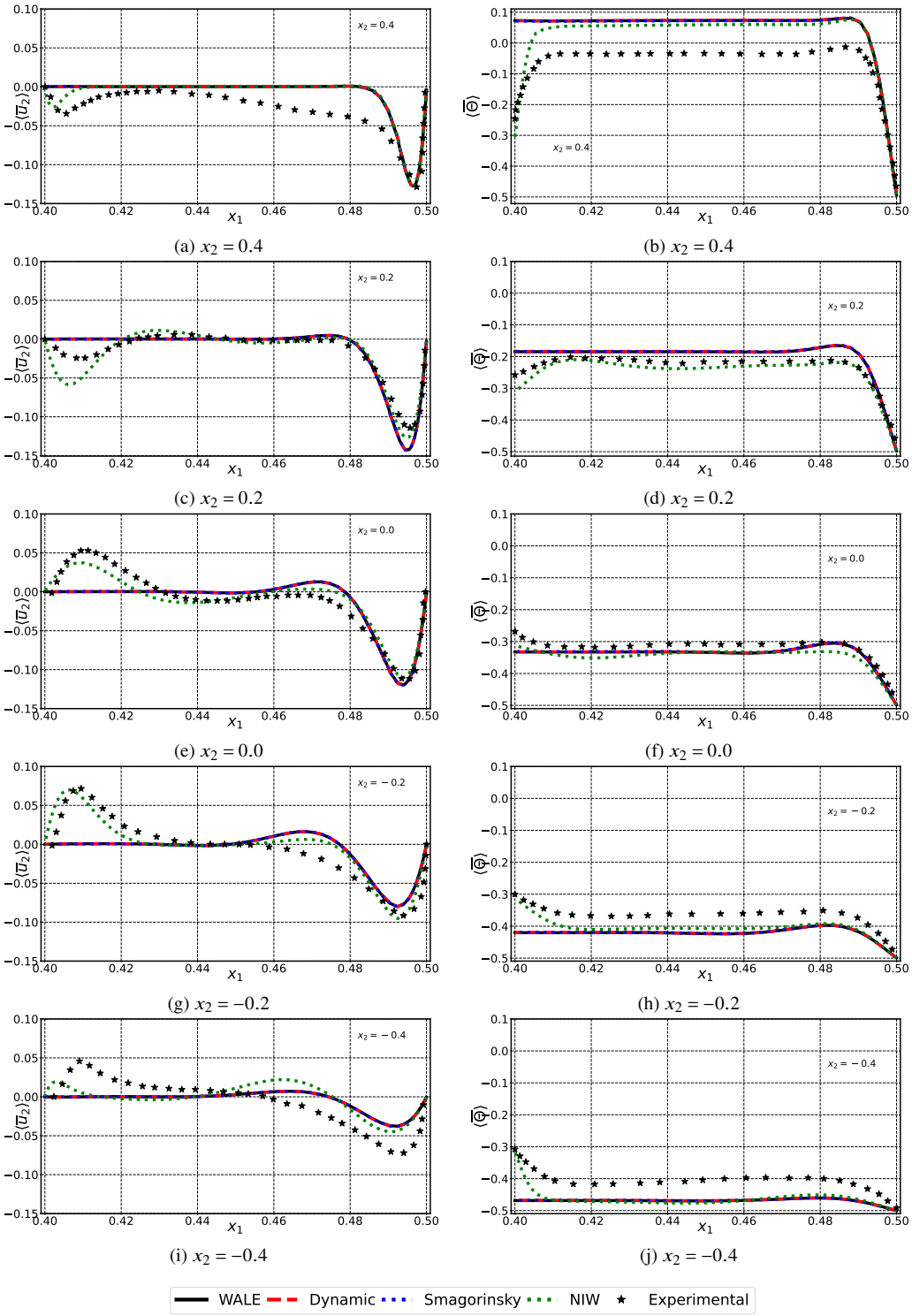

FIG. 8: Horizontal profiles in Zone C. (a), (c), (e), (g), (i): Mean velocity. (b), (d), (f), (h), (j): Mean temperature.

uniform temperature $\overline{\Theta} = -0.3$ is imposed. When NIW replaces the adiabatic condition, the velocity distribution trend is consistent with the experimental findings (Figures 8a, 8c, 8e & 8g). However, this modification is not sufficient to perfectly match the experiments. In particular, the core temperature in the lower part of Zone C is still underestimated, such that the temperature of the flow that enters Zone A (Figure 5i) is still underestimated, which affects the initial velocity in the boundary layer along the hot wall. This numerical experiment brings strong evidence that the differences between LES

results and experimental data are due to the impossibility of obtaining ideal conditions experimentally. To reproduce these data perfectly, heat fluxes or temperatures would have to be available on all the walls of the experimental cavity.

D. Investigation of the 3D effects

The gaps between the front and rear wall of the cavity and the obstacle appears passive but plays a vital role. This section is aimed at revealing the effects of the end walls located at $x_3 = \pm 0.5$ on the flow structure and thermal distribution in the cavity, by means of a new numerical experiment, illustrated by Figure 9. In the periodic approximated cavities (PACs), the solution is assumed to be periodic in the spanwise direction, and three different thicknesses, $\Delta x_3 = 0.05$, $\Delta x_3 = 0.1$ and $\Delta x_3 = 0.2$, are considered. In contrast, in the fully realistic cavity (FRC), the full geometry is considered, and adiabatic and non-slip boundary conditions are imposed on the end walls of the obstacle and the cavity. LES using the WALE model is performed in both FRC and PAC, and the effect of the presence of the end walls is shown for Zone A in Figure 10. For $x_2 \geq 0$, PAC underestimates the flow in the vicinity of the hot wall, while FRC has a close agreement with the experiment (Figure 10a, 10c & 10e). In the vicinity of the cold wall, both PAC and FRC give a good prediction of the average velocity. However, rather surprisingly, PAC gives a better velocity profile in the core of the flow at $x_2 = 0.4$, while the temperature profiles are not as good. At $x_2 = -0.2$, PAC and FRC produced identical velocity and thermal fields (Figure 10g & 10h). At the entrance of Zone A, $x_2 = -0.4$, PAC produces a higher hydrodynamic boundary layer thickness than FRC, which is also quite unrealistic (Figure 10i). End wall effects at $x_3 = \pm 0.5$ work as a flow damper for FRC, which is missing for PAC and results in the formation of this thick hydrodynamic boundary layer at the entrance of Zone A (Figure 10i). The artificial periodic boundary condition for PAC also results in a higher overestimation of the temperature field for $x_2 \geq 0$ than FRC (Figure 10b, 10d & 10f). Simulations with PAC are computationally cheaper than FRC, but PAC is not the substitute for FRC for flow prediction because the absence of the front and rear wall produces discrepancy in an average flow field and has different mechanisms for flow transition to turbulence. This point is discussed extensively in the next section.

E. Thermal Stratifications & Heat Transfer

Figures 11a & 11b represent the thermal stratification in Zone A and C, respectively. The FRC simulation gives a linear stratification in Zone A, up to $x_2 = 0$, within the 99% confidence interval indicated on the figure, with a slope similar to the one observed in the experiments, contrary to the PAC simulation (Figures 11a). However, since, as explained above, the flow entering Zone A from Zone D is at a too low temperature, the curve in Figure 11a is shifted towards the left in the lower part of Zone A. A nonlinear thermal stratification develops due to the fact that the flow becomes more complex than two separated boundary layers. Nonlinear stratification reduces the overall heat transfer in a system, as the temperature gradients are less steep. Thermal stratification for PAC in the lower part of Zone C closely matches the experimental stratification (Figures 11b). However, it deviates largely towards the upper half of the cavity from the experiment compared to the FRC.

Heat fluxes are measured along the hot and cold walls of Zone A and represented in terms of Nusselt number. The Nusselt number for the present configuration is defined as

$$Nu\,(x_2) = \frac{H_b}{L}\frac{\partial <\overline{\Theta}>}{\partial x_1}. \tag{13}$$

Figures 11c & 11d show the comparison of the mean Nusselt number along the cold wall and hot wall in Zone A in the central plane at $x_3 = 0$. The mean Nusselt number decreases sharply from the bottom end of the hot wall in the downstream direction. It is less steep for $x_2 \geq -0.2$, which corresponds to the transition process due to amplification of disturbances in the thermal boundary layer, which subsequently disrupts the laminar flow. A relatively hot flow approaches the bottom of the hot wall in the experiment, resulting in less heat exchange at the wall. As a result, the mean Nusselt number is overpredicted compared to the experiment for $x_2 < -0.2$. The Nusselt number for the FRC at the cold wall reasonably matches the experiment (Figures 11d), in contrast with the PAC.

The Brunt–Väisälä frequency, also known as the buoyancy frequency, is the frequency at which a fluid particle would oscillate if it were displaced from its equilibrium position in a fluid with stable density stratification. It involves the potential temperature of the fluid and its vertical gradient, and is expressed as

$$f_{bv} = \frac{1}{2\pi}\sqrt{\frac{g\beta(T_H - T_C)}{L}\frac{\partial <\overline{\Theta}>}{\partial x_2}}. \tag{14}$$

A stably stratified core region sustains internal gravity waves, which are characterized by the Brunt–Väisälä frequency (see, for instance, Patterson and Imberger[62]). Thorpe[63] calculated the wave profiles and eigenfrequencies of the oscillations for standing internal gravity waves in an inviscid, continuously stratified medium. Turner and Turner[64] reported that the Brunt–Väisälä frequency also represents the frequency of travelling internal gravity waves. These travelling waves occur in the presence of a localized energy source, like the hot wall, from where the waves travel away. f_{bv} corresponds to the frequency of the fundamental mode[65] and represents an upper bound for all possible wave patterns. When the stratified fluid is excited with a particular frequency f for $f < f_{bv}$, the internal waves propagate with an angle $\theta = \arcsin(f/f_{bv})$ with the vertical direction. For the FRC simulation, the linear stratification has a non-dimensional slope of 0.33, which rapidly increases in the nonlinear zone for $x_2 > 0$. Strong recirculation at the top of Zone A controls the stratifications at these elevations in the core. A range of $f_{bv} = 0.01 - 0.18$ is obtained from the corresponding temperature gradients at different elevations. This indicates the possibility of multiple horizontally propagating internal waves in the core. The characteristic frequency of any standing wave pattern in a vertical direction should be between $\frac{f_{bv}}{\sqrt{2}}$ and f_{bv}.[65] The frequencies of the gravity waves are computed at the vertical midplane

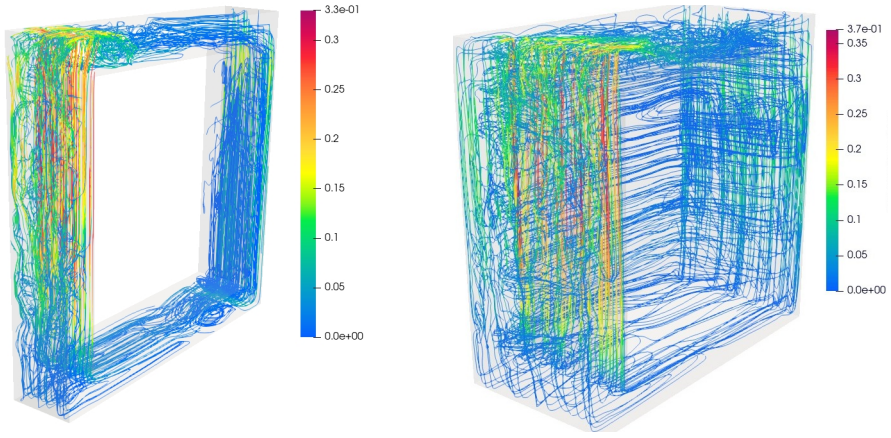

(a) (b)

FIG. 9: Streamlines (WALE model). (a) PAC, (b) FRC.

($x_1 = -0.45$) from the FFT of the fluctuations in vertical velocity u_2' at different elevations. The time series and power spectra of u_2' are provided in Figure 12. The power spectra exhibit peaks at frequency $f_{bv} \approx 0.1$, which is within the predicted range. The flow is however complex, and a unique and well-defined wave pattern is not anticipated. Figure 13b represents the normalized cumulative power spectrum density for points at different altitudes along the vertical mid-plane of Zone A. A broadband spectrum of 5×10^{-3} to 5 is part of internal waves. Figure 13c represents the standard deviation of the velocity fluctuations at different altitudes for $x_1 = -0.45$. Standard deviation for u_2' is minimum at $x_2 = -0.35$ and maximum at $x_2 = 0.45$. Figures 13b and 13c both show the development of broadband fluctuations, indicating that turbulence appears gradually in the differentially heated vertical channel of Zone A. The moments of these fluctuations are studied in the next section.

F. Second-order flow statistics

The second-order flow statistics are now considered in order to identify how the fluctuations develop in the boundary layers along the walls. For this purpose, Fig. 14 shows, in the symmetry plane, the non-zero components of the Reynolds-stress tensor $< u_i' u_j' >$, as well as the anisotropy tensor and its principal invariants. The components available in the experimental database, $< u_1'^2 >$, $< u_2'^2 >$ and $< u_1' u_2' >$ are plotted for comparison. Only the profiles extracted in the upper part of the vertical channel are plotted here for conciseness, since, as will be seen soon, transition to a fully developed turbulence occurs between the vertical locations $x_2 = 0.4$ and $x_2 = 0.5$. The experimental data show that along the cold wall, located at $x_1 = -0.5$, the flow is fully turbulent: indeed, as expected in a turbulent boundary layer (see, for instance, Schlatter *et al.* [67]), the streamwise component $< u_2'^2 >$ is dominant, as it is essentially the one that receives the energy transferred from the mean motion to the turbulent motion via the dominant production term $P_{22} = -2 < u_1' u_2' > \partial < \overline{u_2} > / \partial x_1$; the $< u_1'^2 >$ component (as well as the $< u_3'^2 >$ component which was not measured), receives energy via the redistribution term (pressure-strain correlation); $< u_1' u_2' >$, which is the dominant term in the streamwise momentum balance, is of opposite sign to the gradient $\partial \overline{u_2} / \partial x_1$. The situation is different along the hot wall located at $x_1 = -0.4$: it can be seen that, at the vertical position $x_2 = 0.4$ (Fig. 14a), $< u_1'^2 >$ and $< u_1' u_2' >$ are virtually zero, while the streamwise component $< u_2'^2 >$ is very energetic. This situation is characteristic of the Klebanoff modes[68] observed in bypass transition, i.e., structures elongated in the streamwise direction (streaks) appearing in the streamwise component of the fluctuating field.[69] This suggests that up to the position $x_2 = 0.4$, the boundary layer is not a fully developed turbulent boundary layer since it essentially exhibits streamwise fluctuations. As will be discussed in section III G, the transition mechanisms in the boundary layer along the vertical wall can be more complex than those at work in a classical flat plate boundary layer, such that the streamwise streaks are denoted as *Klebanoff-like* modes here. Fig. 14b shows that at the uppermost measurement position, the flow has finally become turbulent, with $< u_1'^2 >$ and $< u_1' u_2' >$ components that have become significant.

Fig. 14 also shows the results obtained in the FRC using the WALE model (as shown in section III C, the results are identical for the other models). Relatively close agreement is seen along the cold wall, although $< u_2'^2 >$ is overestimated. Close to the hot wall, at position $x_2 = 0.4$, a transitional boundary layer is observed as in the experiments, with an overestimation of the streamwise fluctuations. At $x_2 = 0.5$, while the experimental data show that the boundary layer is clearly a fully developed turbulent boundary layer, this transition is still in progress in the LES. One can clearly identify this behavior by looking at the anisotropy tensor defined by

$$b_{ij} = \frac{< u_i' u_j' >}{2k} - \frac{1}{3}\delta_{ij}, \tag{15}$$

where $k = < u_i' u_i' > /2$ is the turbulent energy. At the cold wall, as expected for a turbulent boundary layer, the streamwise component b_{22} is dominant, the b_{33} component is weaker,

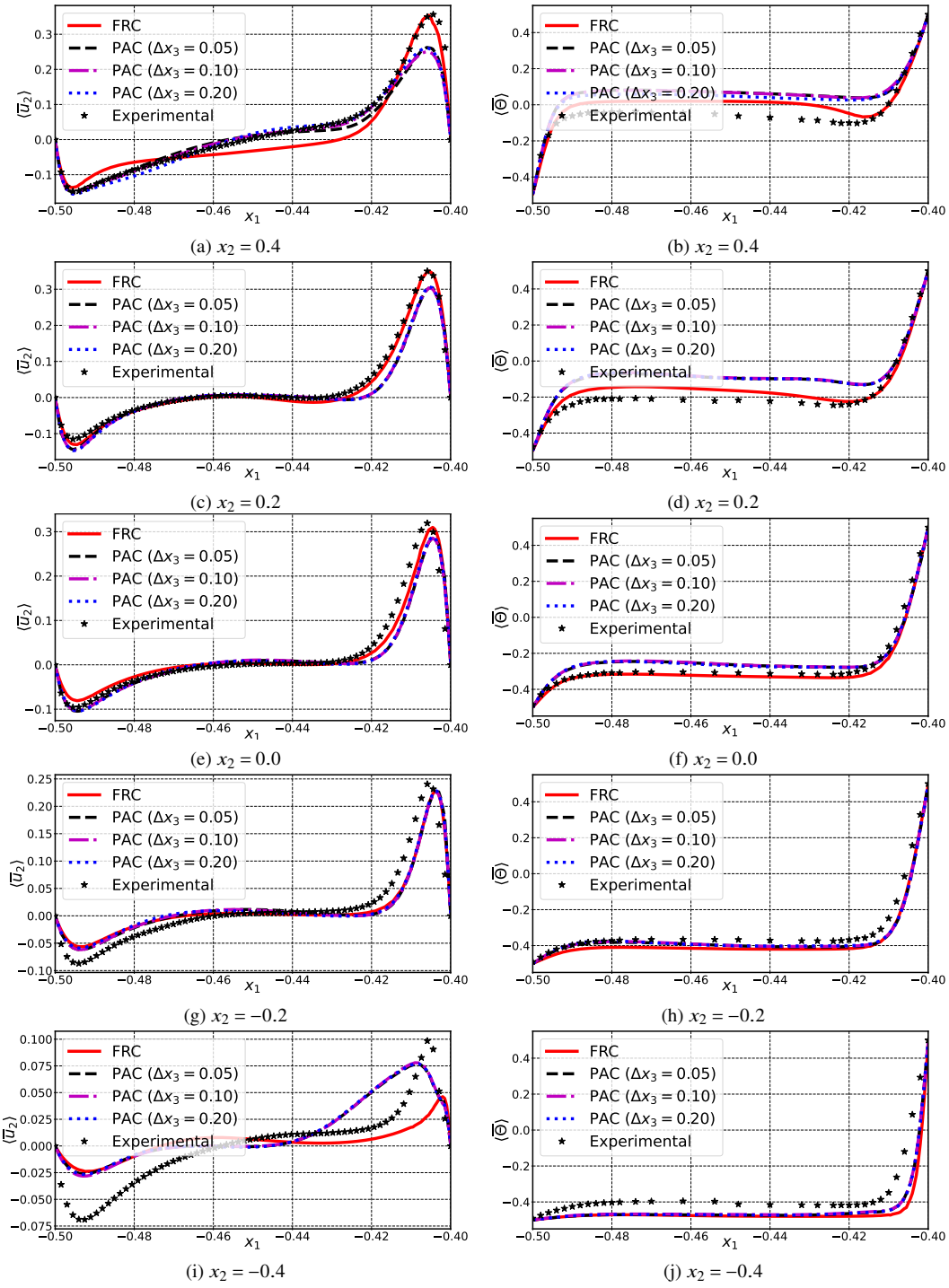

(a) $x_2 = 0.4$ (b) $x_2 = 0.4$

(c) $x_2 = 0.2$ (d) $x_2 = 0.2$

(e) $x_2 = 0.0$ (f) $x_2 = 0.0$

(g) $x_2 = -0.2$ (h) $x_2 = -0.2$

(i) $x_2 = -0.4$ (j) $x_2 = -0.4$

FIG. 10: Comparison of velocity and temperature profile in zone A for FRC and PAC (WALE). (a), (c), (e), (g), (i): Mean velocity. (b), (d), (f), (h), (j): Mean temperature.

and b_{11} tends to $-1/3$ at the wall, because, due to the blocking effect,[70] the fluctuations normal to the wall tend to zero faster than the others,[71] which leads to the two-component limit of turbulence. On the other hand, near the hot wall, we can clearly see at $x_2 = 0.4$ that the two components b_{11} and b_{33} are $-1/3$ over the whole thickness of the boundary layer (up to the velocity peak), and that $b_{12} = 0$: these values are characteristic of a fluctuating energy carried only by fluctuations in the streamwise direction, and thus of Klebanoff-like modes. At $x_2 = 0.5$, we see that the transition to a fully developed turbulence is not accomplished yet, as the b_{12} component is non-zero, but b_{11} and b_{33} remain equal to $-1/3$.

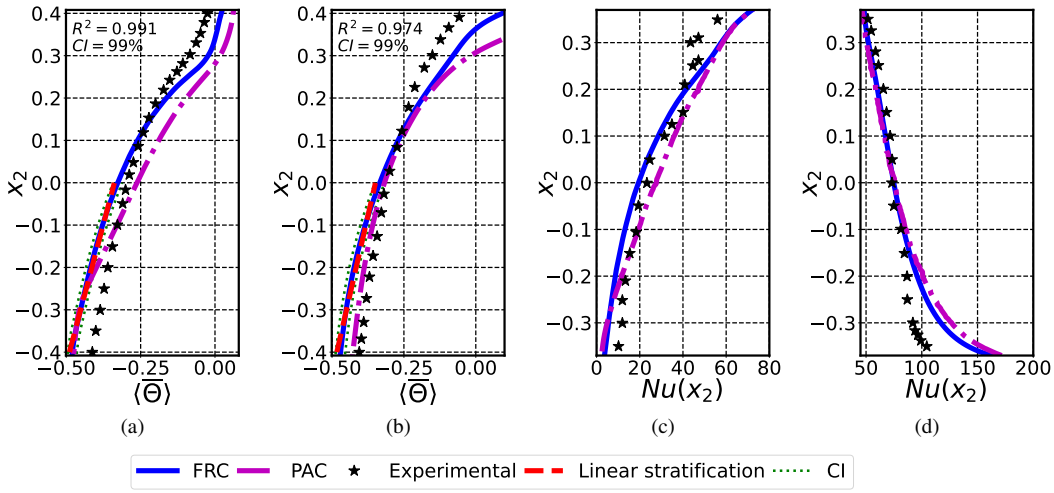

FIG. 11: Thermal stratification and Nusselt number distributions (a: zone A, b: zone C, c: cold wall, d: hot wall)

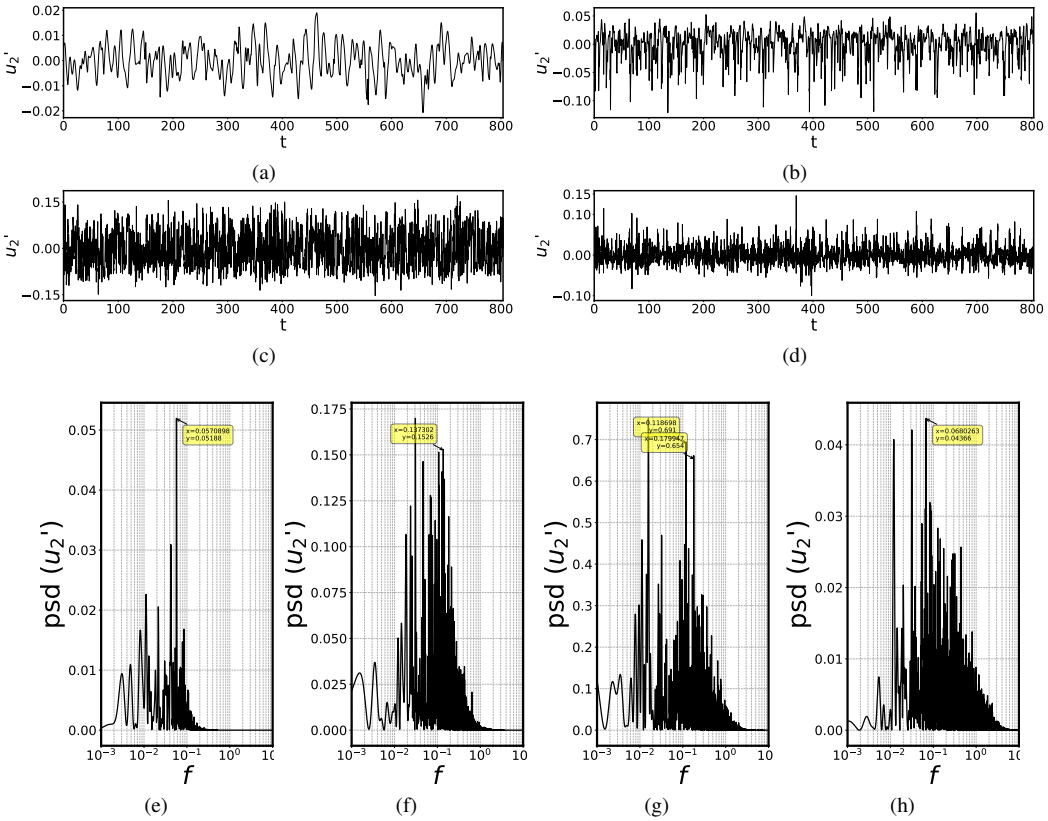

FIG. 12: Time series and power spectral density (psd) in the symmetry plane ($x_3 = 0$) for: (a) and (e) p-0 (-0.45, -0.35), (b) and (f) p-3 (-0.45, 0.05), (c) and (g) p-7 (-0.45, 0.45), (d) and (h) p-11 (-0.45, 0.49)

An even clearer way to visualize the laminar and turbulent regions is to plot Lumley's invariant map, shown in Fig. 14 (bottom). The principal invariants of the anisotropy tensor $\mathbf{b}$ are defined as

$$I = \{\mathbf{b}\} = 0\,, \quad II = -\frac{\{\mathbf{b}^2\}}{2} \text{ and } III = \frac{\{\mathbf{b}^3\}}{3}\,, \qquad (16)$$

where $\{.\}$ denotes the trace. Lumley[72] showed that, the Reynolds-stress tensor being a positive semi-definite tensor, at any point of the flow, in the invariant map which plots $-II$ as a function of III, the points necessarily remain inside the triangle drawn in Fig. 14 (bottom). The lines bounding this

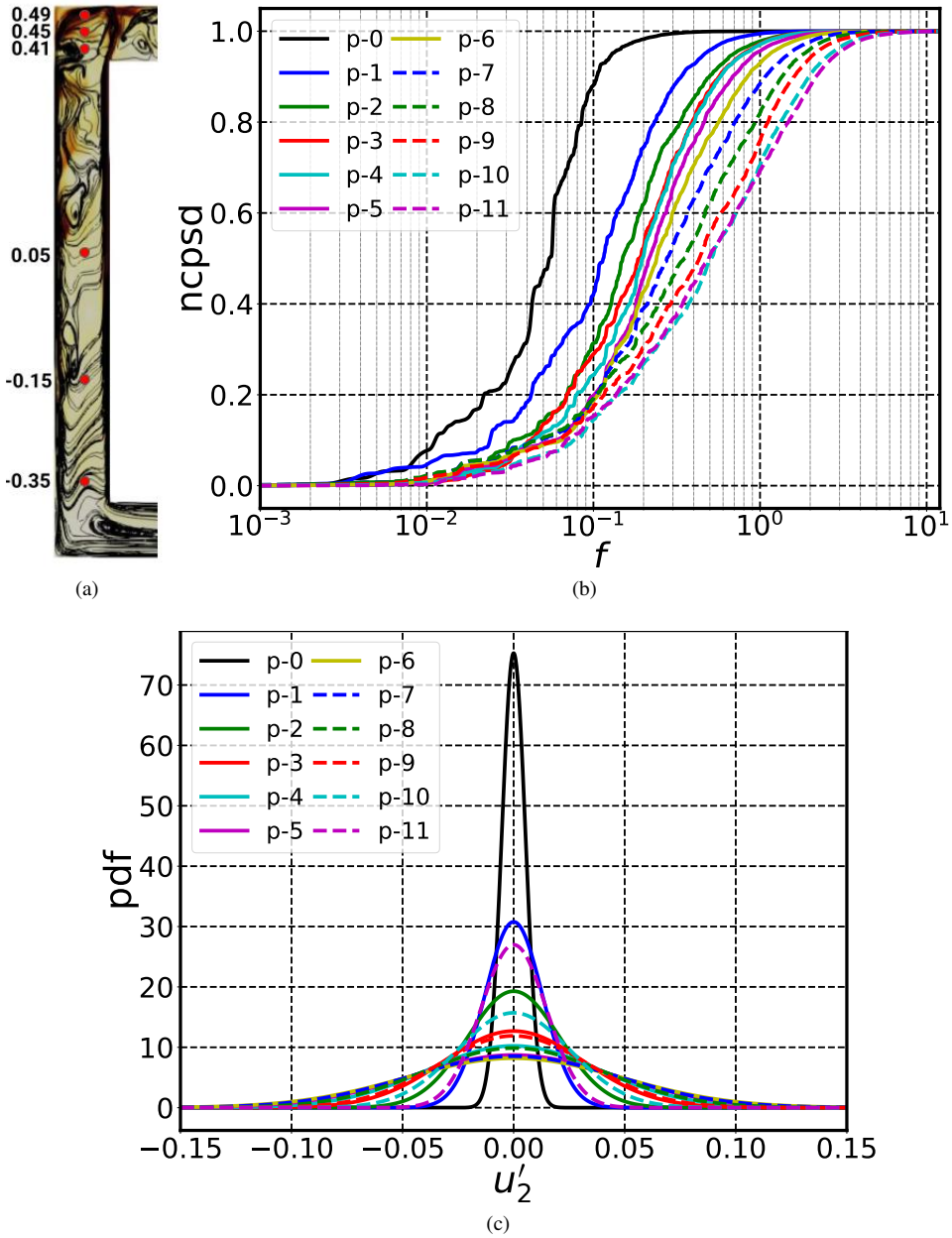

FIG. 13: (a) View of Zone A. (b) Normalized cumulative power density distribution for u_2'. (c) Probability density function for u_2' (points from p-0 to p-11 are taken in the middle of the channel ($x_1 = -0.45$), in the symmetry plane ($x_3 = 0$) and at $x_2 = -0.35, -0.15, 0.05, 0.41, 0.42, 0.43, 0.44, 0.45, 0.46, 0.47, 0.48, 0.49$, respectively.)

triangle are defined by

$$G = \frac{1}{9} + 3III + II = 0\,; \quad H = \frac{III}{2\,(-II/3)^{3/2}} = 1 \text{ and } \; H = -1, \tag{17}$$

as indicated in the figure. The point where $II = 0$ and $III = 0$ indicates isotropic turbulence; the $H = 1$ line, axisymmetric turbulence with one dominant component (two eigenvalues of the Reynolds-stress tensor are equal and smaller than the third); the $H = -1$ line, axisymmetric turbulence with one dominated component (one eigenvalue is smaller than the other two, which are equal); the $G = 0$ line, the two-component limit (one eigenvalue is zero). When extracting the data along a horizontal profile, the trajectory in this invariant map does not follow the one expected for developed turbulence. For comparison, the trajectory obtained along a horizontal profile extracted at mid-height in a square cavity with fully turbulent boundary layers[66] is also plotted. If we follow this trajectory starting from the wall and gradually mov-

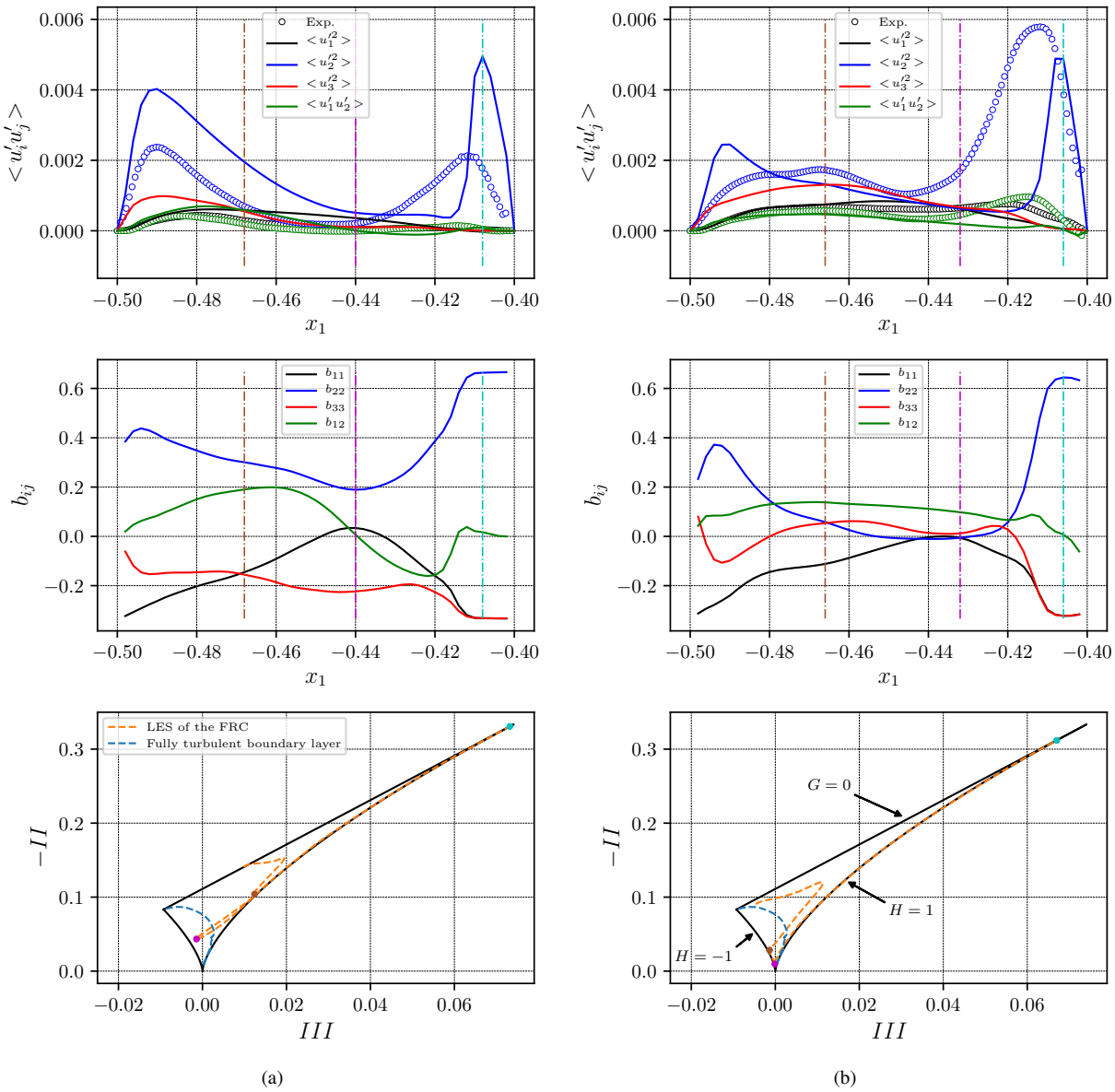

(a) (b)

FIG. 14: Second-order flow statistics for FRC (WALE). Top: Reynolds-stress tensor $\overline{u_i u_j}$; Middle: Anisotropy tensor b_{ij}; Bottom: Lumley's invariant map. In the invariant map, the three particular points correspond to the positions identified by vertical lines of the same color in the other figures, and the blue dashed line corresponds to the DNS of a fully turbulent boundary layer along a vertical hot wall.[66] (a) $x_2 = 0.4$, (b) $x_2 = 0.5$.

ing away from it, we observe this evolution: at the wall, the curve starts from the corner of the triangle corresponding to an axisymmetric, two-component turbulence (the component normal to the wall being negligible); when we move away from the wall, the streamwise component is stronger than the two others and the curve shifts to the right; far from the wall, turbulence becomes isotropic, and the curve approaches the point $(0,0)$. The LES in the FRC case shows a completely different trajectory, which can now be followed from the cold wall to the hot wall: moving away from the cold wall, we observe a trajectory similar to the one seen before, until we obtain an almost isotropic turbulence, at the point identified by the purple dot; moving in the direction of the hot wall, the two components $< u_1'^2 >$ and $< u_3'^2 >$ are almost equal and much smaller than the $< u_2'^2 >$ component, so that the trajectory follows the line $H = 1$; these two components fall to zero at the point identified by a light blue point, which is close to the tip of the triangle that corresponds to a one-component fluctuating field, characteristic of Klebanoff-like modes. The brown point is a reference point, on the cold side, where the turbulence is perfectly axisymmetric: at $x_2 = 0.4$, we have $< u_1'^2 >=< u_3'^2 >< < u_2'^2 >$, so that $H = 1$; at $x_2 = 0.5$, we have

$< u_1'^2 > < < u_2'^2 > = < u_3'^2 >$, so that $H = -1$.

The analysis of the profiles of the Reynolds stresses and the components of the anisotropy tensor, as well as of the trajectories in the invariant map, shows that the turbulent boundary layer along the hot wall is not fully developed until the $x_2 = 0.5$ position, and that this development takes place slightly later in the LES than in the experiment. The following section is devoted to the study of the transition mechanisms of this boundary layer.

G. Flow Instability and Transition to Turbulence

Capturing the transition to turbulence using DNS and LES has been studied extensively for natural convection in cavities.[31,73–75] This section presents the mechanism of instability and transition from laminar to chaotic flow, along with the results obtained from this study.

Paolucci and Chenoweth[73] showed that for a high aspect ratio (≥ 3) cavity, the transition to turbulence results from sidewall boundary layer instability, and for a small aspect ratio (< 3) cavity, transition is due to internal waves near the departing corners. Janssen and Henkes[75] also reported the instability developed in the boundary layers for cavity flow. Boundary layers developed along the isothermal, vertical walls of the cavity resemble those along an isolated, heated vertical plate. A travelling waveform in the cross-stream direction, similar to the Tollmien-Schlichting (TS) waves observed in forced convection, disrupts the laminar boundary layer and results in a transition to chaos. These waves are typically caused by viscosity and a velocity gradient in the boundary layer, which results from an imbalance between the pressure and the shear stress in the fluid. This imbalance leads to the growth of disturbances of a specific wavelength and disrupts the laminar boundary layer.[76] Several experimental and numerical studies have been performed on the natural convection boundary layers along an isolated vertical plate. Jaluria and Gebhart,[77,78] and Gebhart[79] have experimentally studied the transition of the natural convection boundary layer for water along a vertical plate with isothermal and uniform wall-heat flux conditions. Dring and Gebhart[80] solved the Orr-Sommerfield equations to analyze the linear stability and reported that the low-frequency disturbances become unstable first and amplify very slowly. The higher frequency, shorter wavelength disturbances amplify much faster, and become the dominant ones. Qureshi and Gebhart[81], Mahajan and Gebhart[82] found that the periodic waves in the boundary layers are filtered into a single frequency amplified wave downstream of the boundary layer. This single frequency is independent of the position in the downstream direction and is known as characteristic frequency.[78] This second fundamental frequency is present only in the vicinity of the vertical isothermal/uniform heat flux walls. Solution of the Orr-Sommerfeld equation for supercritical Rayleigh number gives a spectrum of unstable modes instead of a single frequency.[83] Complex geometric configurations often results from the superposition of harmonic disturbances and the missing of distinct frequency TS waves. The boundary layer formed in the cavity differs from the boundary layer formed along an isolated vertical plate: for isolated vertical plates, the instability is mainly buoyancy-driven, whereas instability in the isothermal walls of the cavity is both buoyancy and shear-driven. Often TS waves are damped by viscous dissipation and thermal diffusion, and, the flow undergoes bypass transition to turbulence.

Flow passes through an early transition to turbulence after encountering a sharp corner or a sharp edge in natural convection.[31] The enhanced buoyancy effect destabilizes the flow and leads to the formation of small-scale three-dimensional turbulent structures in the boundary layer that suppress the growth of TS waves. This bypass transition (also known as hydraulic jump) results when a vertical boundary layer hits the horizontal wall and bends to a horizontal layer and vice versa.[73] This hydraulic jump mechanism for early transition to turbulence was not very clear and Ravi, Henkes, and Hoogendoorn[84] found the thermal mechanism responsible for bypass transition at a corner rather than internal hydraulic jump. Janssen and Henkes[75] noticed a Kelvin-Helmholtz type shear-driven bifurcation of the flow at the corners of a square cavity which results in flow transition in periodic and quasi-periodic flow regimes.

The thermal and hydrodynamic boundary layer grows along the vertically heated wall of the obstacle resulting in a rapid change in velocity and temperature in this thin layer. Figure 15 represents isocontours of the Q-criterion. The forced periodic boundary condition for PAC results in an unsteady boundary layer characterized by two-dimensional vortices aligned with the spanwise direction and advected in the streamwise direction: the shear layer develops a viscous instability of TS type in the streamwise direction due to the growth in the amplitude of the external disturbances. Figure 16 shows the power spectral density measurements in the vicinity of the hot wall. Up to the midplane ($x_2 = 0$), the boundary layer sustains only internal low-frequency waves (Figure 16b). Above the midplane, at $x_2 = 0.15$, another frequency of 1.96 starts growing in the vertical boundary layer (Figure 16c). At $x_2 = 0.3$, the TS waves dominate the power spectrum (Figure 16d). From $x_2 = 0.3$, the breakdown process starts: these TS waves break into three-dimensional vortices (Figure 15b).

In contrast with the PAC that promotes the appearance of spanwise, TS like structures, the presence of the front and rear walls results in an unsteady three-dimensional boundary layer from the beginning of the lower corner for FRC (Figure 15d). Due to the presence of the end walls and the lateral channels, the streamlines are 3D (Figure 9b) and some fluid moves perpendicularly to the ascending boundary layer along the hot wall. This secondary flow is called the crossflow (CF), and the three-dimensional boundary layer can be affected by a crossflow instability (CFI) transition. Crossflow instabilities manifest as contiguous corotating vortices (CFVs), which develop inside the three-dimensional boundary layer in a direction closely aligned with the external inviscid flow.[85] These vortices can remain stationary or travel along the spanwise direction depending on the disturbance level outside of the boundary-layer flow.[86–88] This results in a modulated three-dimensional boundary layer which is highly unstable and affected by the secondary instabilities, which rapidly amplify, leading to the breakdown of the CF vortices and the laminar-

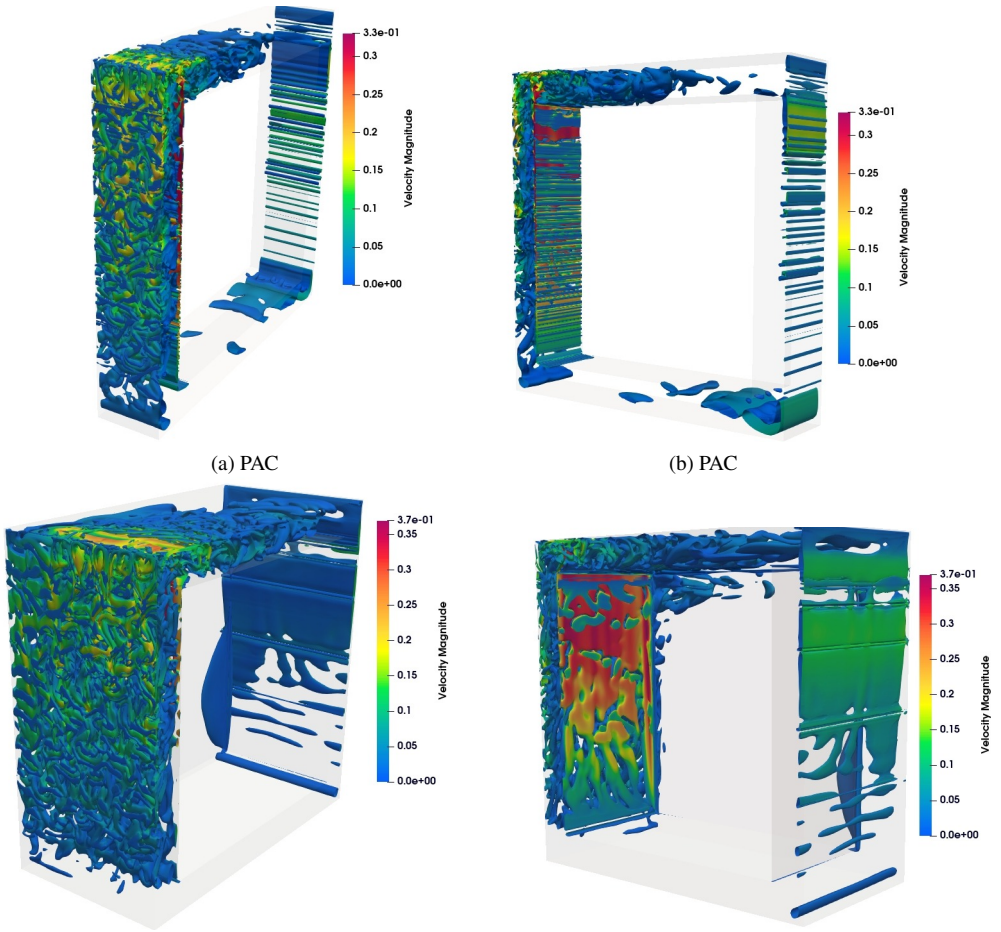

(a) PAC (b) PAC

(c) FRC (d) FRC

FIG. 15: Isocontours of the Q-criterion colored by the velocity magnitude for: (a) and (b) PAC and (c) and (d) FRC (WALE model)

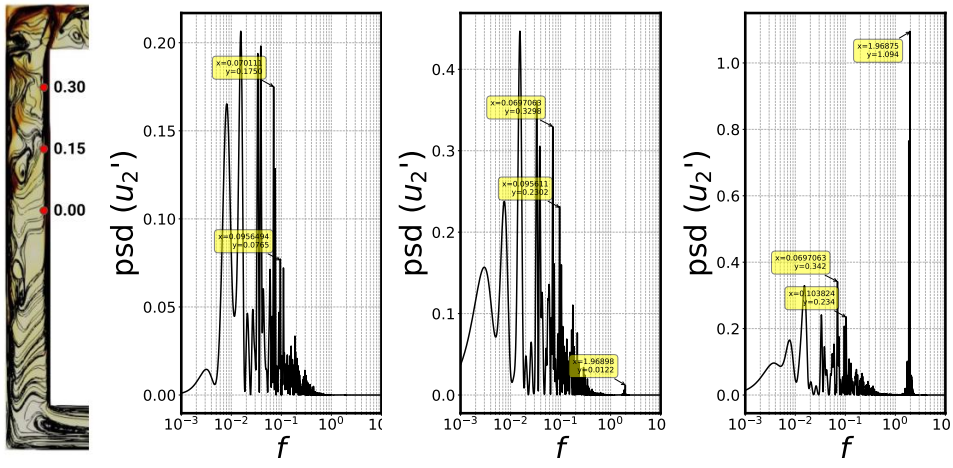

(a) (b) (c) (d)

FIG. 16: Power spectral density at points in the boundary layer near the hot wall ($x_1 = -0.41$) in the symmetry plane ($x_3 = 0$) for the PAC simulation. (a) View of Zone A. (b) $x_2 = 0$. (c) $x_2 = 0.15$. (d) $x_2 = 0.3$.

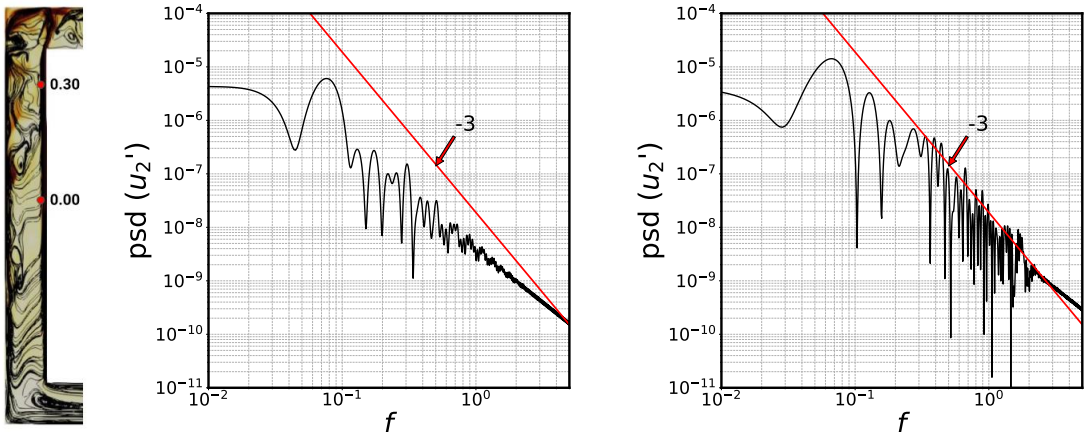

FIG. 17: Power spectral density at points in the boundary layer near the hot wall ($x_1 = -0.4025$) for FRC simulations in the symmetry plane ($x_3 = 0$). (a) View of Zone A. (b) $x_2 = 0$. (c) $x_2 = 0.3$.

turbulent transition,[87–89] which can be observed in Figure 15 and identified by looking at the Reynolds-stresses in Figure 14.

Moreover, this transition to turbulence is confirmed by the power spectra in Figure 17, which exhibit broadband characteristics very different from the spectra observed for the PAC in Figure 16. For fully buoyancy-driven turbulent flows, the power spectral density decays with a slope of -3 for a quite large frequency range.[90] Figure 17 represents the psd of the vertical velocity fluctuations at different altitudes along the thermal boundary layer. At the early stage of transition, the energy spectrum does not exhibit an intertial range, as can be seen at $x_2 = 0.0$ (Figure 17c). When nonlinear interactions gradually generate smaller and smaller structures, the energy is more widely distributed over a large frequency range, and the inertial subrange arises. At $x_2 = 0.3$, the psd has a slope of -3, which indicates the transition towards a turbulent natural convection boundary layer.

It can be concluded that there are profound differences between the dynamics observed in the PAC and in the FRC. The difference in first-order statistics of velocity and temperature for FRC and PAC is reasonable. However, they behave very differently in terms of the mechanisms of transition to turbulence. For practical applications where the average velocity and temperature are of paramount interest, the effects of end walls can be omitted to avoid expensive computation, and this can give mean fields with reasonable accuracy. However, the gain in computational effort is probably not worth the loss of physical representativity. The PAC is computed with 9.5 million cells, while the FRC is computed with 34 million cells. The CPU time necessary for the FRC in our case was around 192,000 hours. The effort is reduced by a factor of only 4 for the PAC (46,000 CPU hours).

H. Chaos Signature from the Time Series Analysis

The transition to turbulence along the hot wall for FRC is noticed in the previous section. Additional testing is done with the time series obtained at the discrete location in the boundary layer to identify the signature of chaos during transitional motion. A phase portrait at $x_2 = -0.35$ is constructed from the fluctuations u_1' and u_2' (Figure 18b). Multiple crossovers in this attractor represent multiple incommensurate frequencies. The intricate geometric pattern in this strange attractor (Figure 18b) represents the hallmark of a chaotic dynamical system. Three-dimensional phase-space for u_2' is reconstructed from an infinitesimal time-delay as shown in Figure 18c. The disorganized emerged pattern in the orbit of the attractor led to identical conclusions for the onset of chaos in the boundary layer. So this phase-space analysis confirms the early appearance of a chaotic motion near the departed corner at $x_2 = -0.3$, which is the first step towards turbulence.

The autocorrelation function (ACF) of a variable is a statistical measure to quantify the degree of similarity or dependence at different time lags. It is computed as

$$\mathrm{ACF} = \frac{\overline{u_2'(t)u_2'(t+\tau)}}{\overline{u_2'(t)u_2'(t)}} \tag{18}$$

Where τ is the time lag. Figure 19b represents the ACF for vertical velocity fluctuations at different elevations along the hot wall boundary layer. The fully turbulent boundary layer at $x_2 = 0.4$ has the first zero crossing at $t \approx 2.2$, while it is at $t \approx 5$ for the upstream points.

Average mutual information (AMI) is used in the dynamical systems to find the optimum time delay (τ) required to reconstruct phase space. This concept is based on information theory, and the first local minima give the optimum time delay.[91] AMI is a generalized version of the autocorrelation function, which attributes the degree of association or dependence between two events in the dynamical system to influence each other. It is computed as

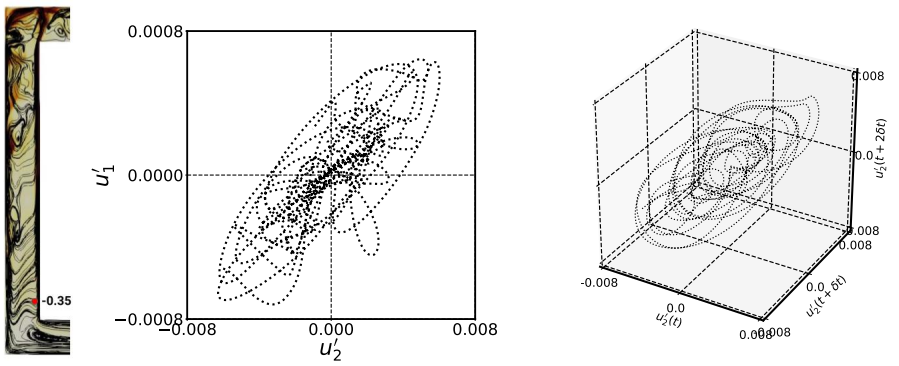

(a) (b) (c)

FIG. 18: Phase portrait and delayed coordinate reconstruction at a point in the upstream of the hot wall boundary layer ($x_2 = -0.35$), close to the wall ($x_1 = 0.4025$) in the symmetry plane ($x_3 = 0$). (a) View of Zone A. (b) Phase plane u_2'–u_1'. (c) Phase space $u_2'(t)$–$u_2'(t+\delta t)$–$u_2'(t+2\delta t)$.

$$\mathrm{AMI}(\tau) = \sum_{u_2'(t_i),u_2'(t_i+\tau)} P\left(u_2'(t_i),u_2'(t_i+\tau)\right) \log_2 \left[\frac{P\left(u_2'(t_i),u_2'(t_i+\tau)\right)}{P\left(u_2'(t_i)\right)P\left(u_2'(t_i+\tau)\right)}\right] \tag{19}$$

Where $P\left(u_2'(t_i)\right)$ and $P\left(u_2'(t_i+\tau)\right)$ are the marginal probabilities, and $P\left(u_2'(t_i),u_2'(t_i+\tau)\right)$ is a joint probability of occurrence of $u_2'(t_i)$ and $u_2'(t_i+\tau)$ in the velocity fluctuation signal. Figure 19c represents the AMI for points at different elevations in the vertical hot wall boundary layer. High altitude points in the boundary layer at $x_2 = 0.2$ and $x_2 = 0.4$ have shorter AMI of ≈ 2. Points in the upstream have AMI ≈ 4.

The geometrical property of a chaotic attractor is reflected in its fractal dimensions (FD), which are the space-filling properties of the process being studied. The fractal dimension of the dynamical system describes the relationship between the variance and the timescale of the time series. The variance drops less rapidly with the increased resolution of the time series when neighbouring elements are positively correlated. In the present analysis, the fractal dimension of the vertical velocity fluctuations in the hot wall boundary layer is computed from Hurst's rescaled range analysis.[92] The Hurst exponent (HE) is a statistical measure used to quantify the long-term memory or persistence of a dynamical system. HE = 0.5 represents a random walk, HE < 0.5 represents anti-persistent and HE > 0.5 represents persistent dynamical system. The dynamic Hurst exponent (DHE) is used to study the time-varying persistence of a dynamical system and detect the changes in the underlying dynamics of a system, such as the transition from a stable to an unstable state. A zero fractal dimension represents a smooth dynamical system, while a fractal dimension of two represents a completely random one. A fractal dimension greater than unity represents a chaotic dynamical system. The fractal dimensions and Hurst exponent are related as FD = 2 – HE.[92] Figure 20b represents the time evolution of the fractal dimensions of points at different altitudes in the vertical boundary layer. All the points have a fractal dimension greater than one, which is again the hallmark of a fully chaotic vertical boundary layer. FD experiences a significant increase between $x_2 = 0.35$ and $x_2 = 0.4$, which is consistent with the scenario elaborated above of a transition to fully developed turbulence in this region.

The phenomenon of recurrence is ubiquitous in dynamic systems. Recurrence refers to the phenomenon where the phase space trajectory may recurve back to the area around its original position after a period of divergence in the phase space. With the use of this property, the time evolution of the system dynamics can be qualitatively captured by the recurrence plot (RP),[93] which represents in a two-dimensional subspace some features of an attractor in higher dimensions. Recurrence plots are quite helpful in discovering underlying complicated patterns in data and providing a visual representation of the dynamical system (Figure 21). The RPs exhibit characteristic large-scale patterns (typology) and small-scale patterns (texture). Chaotic systems form diagonal lines of recurrence as the neighbouring trajectories diverge after a short time of closeness in the phase space.[94] Large patches of black and white spots appear in RP for the dynamical system, which has both fast and slow scales. More isolated black points are formed, moving along downstream. These isolated black points indicate that the evolution of the phase space trajectory is unpredictable at the next instance of time. In this, the black patches consist of vertical lines representing the trapping of slow varying oscillations in between the fast-evolving dynamics.[95] Again, the appearance of a grainy structures in Figure 21f supports the scenario of a development of the fully developed turbulent boundary layer around $x_2 = 0.4$.

IV. CONCLUSIONS

This study presents LES simulations performed to investigate natural convection in a cavity with a partially heated block at a high Rayleigh number of $Ra = 1.46 \times 10^9$, resulting in the development of a turbulent vertical boundary layer on the heated wall and a complex 3D flow inside the cavity. The results are compared to the recent experimental database of

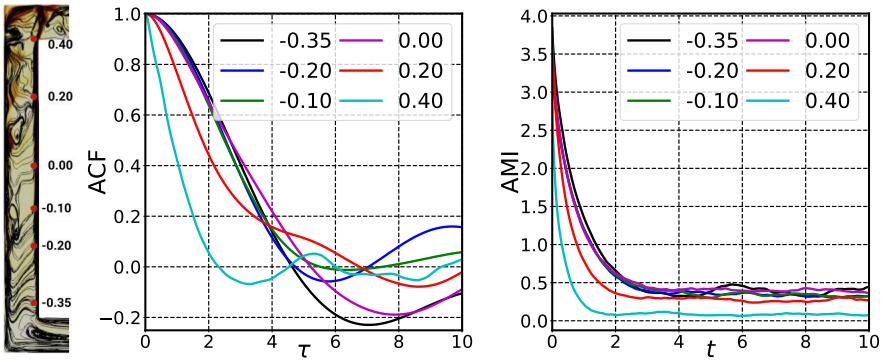

(a) (b) (c)

FIG. 19: (a) View of Zone A. (b) Autocorrelation function (ACF) and (c) average mutual information (AMI) along the vertical hot wall boundary layer .

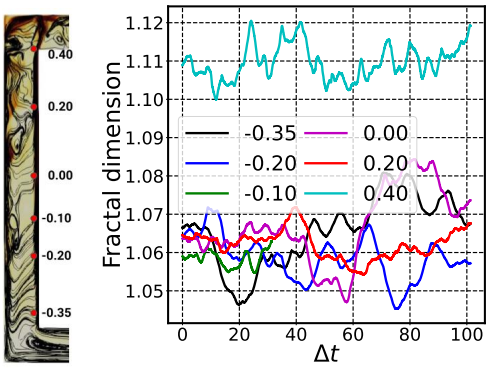

(a) (b)

FIG. 20: (a) View of Zone A. (b) Fractal dimensions for points at different elevations in vertical hot boundary layer.

Weppe, Moreau, and Saury.[12] Although this configuration is a geometric simplification of the flow in an automotive engine compartment, it still captures the essential physical mechanisms that are challenging to model and are present in various industrial configurations and buildings.

The influence of mesh refinement and different types of meshes was examined, leading to the selection of an adequately fine mesh for further analysis. The investigation of the influence of the subgrid-scale model, which is minimal, confirmed the sufficiency of the chosen mesh. As the experimental data did not provide a quantification of the 3D effects on the flow, a numerical experiment was conducted to compare the 3D flow with a statistically invariant flow in the third direction. This study emphasized the significance of considering the effect of the end walls, not only for predicting fluid circulation in the cavity but also for reproducing the transition mechanisms to turbulence. Another parameter affecting the overall fluid circulation in the cavity is the consideration of non-adiabatic conditions due to conduction in the walls of the experimental facility, which can have a significant influence on the global heat transport in the cavity and can require a careful treatment.[96]

Detailed analysis of turbulent statistics and fluctuating velocity spectra revealed the complexity of the flow in the cavity. The geometry induces a three-dimensional boundary layer in which secondary instabilities rapidly amplify, leading to bypass transition. Within the transitional boundary layer, the dynamics is dominated by longitudinal fluctuations resembling Klebanoff modes, and the spectra also exhibit the presence of gravity waves due to thermal stratification. The examination of temporal signals indicated the rapid onset of chaos in the boundary layer and confirmed the transition to fully developed turbulence in the upper region of the boundary layer along the heated wall.

The complexity of this type of flows poses a significant challenge for industrial CFD. In addition to the complexity of the physical mechanisms, which are already present in the simplified geometry studied in this article, many practical applications feature considerable geometric complexity.[97–99] While all the methods used herein (numerical method and LES model) can be applied in these complex geometries, the mesh will have to be finer to represent the geometric details. The transitional nature of the boundary layer on the heated wall, driven by buoyancy effects, makes RANS mod-

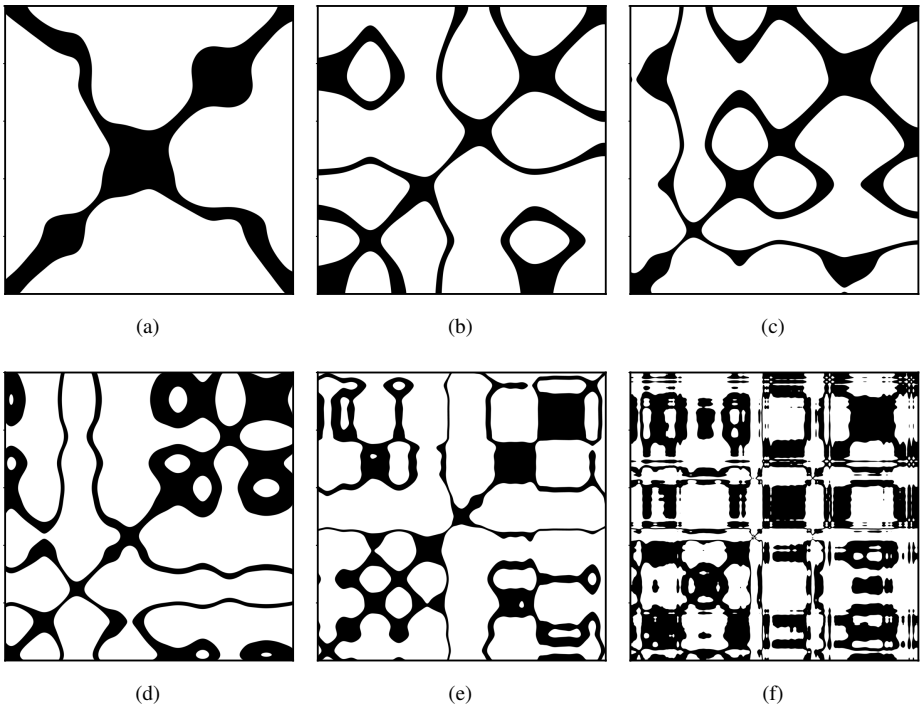

FIG. 21: Recurrence plot of time series signal of u_2' at different altitudes along the hot wall boundary layer, close to the wall ($x_1 = -0.4025$), in the symmetry plane ($x_3 = 0$). (a) $x_2 = -0.35$, (b) $x_2 = -0.20$, (c) $x_2 = -0.10$, (d) $x_2 = 0.00$, (e) $x_2 = 0.20$, (f) $x_2 = 0.40$.

eling particularly difficult. It may require the introduction of buoyancy-specific terms into the eddy viscosity models commonly used in the industry[100] or the utilization of sophisticated Reynolds-stress models.[20] Furthermore, the presence of complex unsteady mechanisms, particularly the interaction between the boundary layer and gravity waves, could justify the use of a LES model, at least locally, advocating for the adoption of the hybrid RANS/LES[101] approach in complex industrial systems.

ACKNOWLEDGEMENTS

This work was supported by ANR via the MONACO_2025 project (ANR-17-CE06-0005-01 ACT). The computations are performed using 1600 parallel cores in GENCI-IDRIS (Grant 2022-A0122A10980) and 640 parallel cores in MCIA (Mésocentre de Calcul Intensif Aquitain) of the University of Bordeaux-UPPA.

REFERENCES

[1] J. M. House, C. Beckermann, and T. F. Smith, "Effect of a centered conducting body on natural convection heat transfer in an enclosure," Numerical Heat Transfer, Part A: Applications **18**, 213–225 (1990).

[2] J. Y. Oh, M. Y. Ha, and K. C. Kim, "Numerical study of heat transfer and flow of natural convection in an enclosure with a heat-generating conducting body," Numerical Heat Transfer, Part A: Applications **31**, 289–303 (1997).

[3] M. Y. Ha, M. J. Jung, and Y. S. Kim, "Numerical study on transient heat transfer and fluid flow of natural convection in an enclosure with a heat-generating conducting body," Numerical Heat Transfer: Part A: Applications **35**, 415–433 (1999).

[4] Y. Liu and N. Phan-Thien, "A complete conjugate conduction convection and radiation problem for a heated block in a vertical differentially heated square enclosure," Computational Mechanics **24**, 175–186 (1999).

[5] M. Y. Ha and M. J. Jung, "A numerical study on three-dimensional conjugate heat transfer of natural convection and conduction in a differentially heated cubic enclosure with a heat-generating cubic conducting body," International Journal of Heat and Mass Transfer **43**, 4229–4248 (2000).

[6] A. Merrikh, "Blockage effects in natural convection in differentially heated enclosures," Journal of Enhanced Heat Transfer **8** (2001).

[7] A. A. Merrikh and J. L. Lage, "Natural convection in an enclosure with disconnected and conducting solid blocks," International Journal of Heat and Mass Transfer **48**, 1361–1372 (2005).

[8] P. Bhave, A. Narasimhan, and D. Rees, "Natural convection heat transfer enhancement using adiabatic block: optimal block size and Prandtl number effect," International Journal of Heat and Mass Transfer **49**, 3807–3818 (2006).

[9] Z. A. Raizah, S. E. Ahmed, and A. M. Aly, "ISPH simulations of natural convection flow in E-enclosure filled with a nanofluid including homogeneous/heterogeneous porous media and solid particles," International Journal of Heat and Mass Transfer **160**, 120153 (2020).

[10] A. M. Aly, "Mixing between solid and fluid particles during natural convection flow of a nanofluid-filled H-shaped cavity with three center gates using ISPH method," International Journal of Heat and Mass Transfer **157**, 119803 (2020).

[11] A. Weppe, F. Moreau, and D. Saury, "Experimental study of a natural convection flow in a cubic enclosure with a partially heated inner block," J. Phys.: Conf. Ser. **2116**, 012033 (2021).

[12] A. Weppe, F. Moreau, and D. Saury, "Experimental investigation of a turbulent natural convection flow in a cubic cavity with an inner obstacle partially heated," International Journal of Heat and Mass Transfer **194**, 123052 (2022).

[13] A. Weppe, *Étude expérimentale d'écoulements turbulents à effets de flottabilité dominants en milieu confiné comportant un obstacle partiellement chauffé*, Ph.D. thesis, ENSMA, Poitiers, France (2022).

[14] A. Weppe, F. Moreau, and D. Saury, "Turbulent natural convection of a confined flow in a cubic enclosure: Effect of transient boundary conditions," Int. Commun. Heat Mass Transfer **142**, 106637 (2023).

[15] N. Ince and B. Launder, "On the computation of buoyancy-driven turbulent flows in rectangular enclosures," Int. J. Heat Fluid Fl. **10**, 110–117 (1989).

[16] R. Henkes, F. Van Der Vlugt, and C. Hoogendoorn, "Natural-convection flow in a square cavity calculated with low-reynolds-number turbulence models," Int. J. Heat Mass Tran. **34**, 377–388 (1991).

[17] S.-H. Peng and L. Davidson, "Computation of turbulent buoyant flows in enclosures with low-Reynolds-number k-ω models," Int. J. Heat Fluid Fl. **20**, 172–184 (1999).

[18] H. S. Dol and K. Hanjalic, "Computational study of turbulent natural convection in a side-heated near-cubic enclosure at a high Rayleigh number," Int. J. Heat Mass Tran. **44**, 2323–2344 (2001).

[19] S.-K. Choi and S.-O. Kim, "Turbulence modeling of natural convection in enclosures: A review," J. Mech. Sci. Technol. **26**, 283–297 (2012).

[20] F. Dehoux, S. Benhamadouche, and R. Manceau, "An elliptic blending differential flux model for natural, mixed and forced convection," Int. J. Heat Fluid Fl. **63**, 190–204 (2017).

[21] S.-K. Choi, J.-W. Han, and H.-K. Choi, "Performance of second-moment differential stress and flux models for natural convection in an enclosure," Int. Commun. Heat Mass Transfer **99**, 54–61 (2018).

[22] Y.-H. Tung, Y.-M. Ferng, R. W. Johnson, and C.-C. Chieng, "Study of natural circulation in a VHTR after a LOFA using different turbulence models," Nuclear engineering and design **263**, 206–217 (2013).

[23] Y.-H. Tung, R. W. Johnson, Y.-M. Ferng, and C.-C. Chieng, "Modeling strategies to compute natural circulation using CFD in a VHTR after a LOFA," Nuclear Engineering and Design **275**, 80–90 (2014).

[24] Y.-H. Tung, R. W. Johnson, Y.-M. Ferng, and C.-C. Chieng, "Bypass flow computations on the LOFA transient in a VHTR," Applied thermal engineering **62**, 415–423 (2014).

[25] Y.-H. Tung, Y.-M. Ferng, R. W. Johnson, and C.-C. Chieng, "Transient LOFA computations for a VHTR using one-twelfth core flow models," Nuclear Engineering and Design **301**, 89–100 (2016).

[26] C. E. Clifford and M. L. Kimber, "Assessment of RANS-Based Turbulence Models for Buoyancy-Influenced Forced Convection on a Heated Vertical Surface," Journal of Verification, Validation and Uncertainty Quantification **5**, 011005 (2020).

[27] A. D. Fradeneck and M. L. Kimber, "Applicability of Common RANS Models for the Calculation of Transient Forced to Natural Convection," Journal of Verification, Validation and Uncertainty Quantification **5** (2020).

[28] S. Jameel, *Turbulence modelling of mixed and natural convection regimes in the context of the underhood-space of automobiles*, Ph.D. thesis, Université de Pau et des pays de l'Adour (2020).

[29] S. Paolucci, "Direct numerical simulation of two-dimensional turbulent natural convection in an enclosed cavity," Journal of Fluid Mechanics **215**, 229–262 (1990).

[30] S. Xin and P. Le Quéré, "Direct numerical simulations of two-dimensional chaotic natural convection in a differentially heated cavity of aspect ratio 4," Journal of Fluid Mechanics **304**, 87–118 (1995).

[31] M. Farhangnia, S. Biringen, and L. Peltier, "Numerical Simulation of Two–Dimensional Buoyancy–Driven Turbulence in a Tall Rectangular Cavity," International journal for numerical methods in fluids **23**, 1311–1326 (1996).

[32] F. Trias, M. Soria, A. Oliva, and C. Pérez-Segarra, "Direct numerical simulations of two-and three-dimensional turbulent natural convection flows in a differentially heated cavity of aspect ratio 4," Journal of Fluid Mechanics **586**, 259–293 (2007).

[33] F. Trias, A. Gorobets, M. Soria, and A. Oliva, "Direct numerical simulation of a differentially heated cavity of aspect ratio 4 with Rayleigh numbers up to 1011–Part I: Numerical methods and time-averaged flow," International Journal of Heat and Mass Transfer **53**, 665–673 (2010).

[34] F. Trias, A. Gorobets, M. Soria, and A. Oliva, "Direct numerical simulation of a differentially heated cavity of aspect ratio 4 with Rayleigh numbers up to 1011–Part II: Heat transfer and flow dynamics," International Journal of Heat and Mass Transfer **53**, 674–683 (2010).

[35] R. Puragliesi, A. Dehbi, E. Leriche, A. Soldati, and M. Deville, "Direct Numerical Simulation of Buoyancy Driven Turbulence inside a Cubic Cavity," in *Turbulence and Interactions*, edited by M. Deville, Lê, Thien-Hiep, and S. Pierre (Springer Berlin Heidelberg, Berlin, Heidelberg, 2010) pp. 295–301.

[36] F. X. Trias, A. Gorobets, A. Oliva, and Pérez-Segarra, "DNS and regularization modeling of a turbulent differentially heated cavity of aspect ratio 5," International Journal of Heat and Mass Transfer **57**, 171–182 (2013).

[37] A. G. Chatterjee, M. K. Verma, A. Kumar, R. Samtaney, B. Hadri, and R. Khurram, "Scaling of a Fast Fourier Transform and a pseudo-spectral fluid solver up to 196608 cores," Journal of Parallel and Distributed Computing **113**, 77–91 (2018).

[38] F. Sebilleau, R. Issa, S. Lardeau, and S. P. Walker, "Direct Numerical Simulation of an air-filled differentially heated square cavity with Rayleigh numbers up to $10^1$1," International Journal of Heat and Mass Transfer **123**, 297–319 (2018).

[39] X. Wen, L.-P. Wang, Z. Guo, and D. B. Zhakebayev, "Laminar to turbulent flow transition inside the boundary layer adjacent to isothermal wall of natural convection flow in a cubical cavity," International Journal of Heat and Mass Transfer **167**, 120822 (2021).

[40] S.-H. Peng and L. Davidson, "Large eddy simulation for turbulent buoyant flows induced by differentially heated vertical walls." (1998).

[41] S.-H. Peng and L. Davidson, "Large eddy simulation for turbulent buoyant flow in a confined cavity," International Journal of Heat and Fluid Flow **22**, 323–331 (2001).

[42] A. Sergent, P. Joubert, and P. L. Quéré, "Development of a local subgrid diffusivity model for large-eddy simulation of buoyancy-driven flows: application to a square differentially heated cavity," Numerical Heat Transfer: Part A: Applications **44**, 789–810 (2003).

[43] D. G. Barhaghi, L. Davidson, and R. Karlsson, "Large-eddy simulation of natural convection boundary layer on a vertical cylinder," International journal of heat and fluid flow **27**, 811–820 (2006).

[44] G. Lau, G. Yeoh, V. Timchenko, and J. Reizes, "Large-eddy simulation of turbulent buoyancy-driven flow in a rectangular cavity," International journal of heat and fluid flow **39**, 28–41 (2013).

[45] N. S. Ghaisas, D. A. Shetty, , and S. H. Frankel, "Large eddy simulation of thermal driven cavity: Evaluation of sub-grid scale models and flow physics," International Journal of Heat and Mass Transfer **56**, 606–624 (2013).

[46] C. Bosshard, A. Dehbi, M. Deville, E. Leriche, R. Puragliesi, and A. Soldati, "Large eddy simulation of the differentially heated cubic cavity flow by the spectral element method," Computers & Fluids **86**, 210–227 (2013).

[47] D. Kizildag, F. Trias, I. Rodríguez, and A. Oliva, "Large eddy and direct numerical simulations of a turbulent water-filled differentially heated cavity of aspect ratio 5," International Journal of Heat and Mass Transfer **77**, 1084–1094 (2014).

[48] Z. Zhang, W. Chen, Z. Zhu, and Y. Li, "Numerical exploration of turbulent air natural-convection in a differentially heated square cavity at $Ra = 5.33 \times 10^9$," Heat and Mass Transfer **50**, 1737–1749 (2014).

[49] R. Kumar and A. Dewan, "A study of LES–SGS closure models applied to a square buoyant cavity," International Journal of Heat and Mass Transfer **98**, 164–175 (2016).

[50] M. Sayed, M. Hadžiabdić, A. Dehbi, B. Ničeno, and K. Mikityuk, "Simulation of flow and heat transfer in a differentially heated cubical cavity using coarse Large Eddy Simulation," International Journal of Thermal Sciences **183**, 107892 (2023).

[51] J. Salat, S. Xin, P. Joubert, A. Sergent, F. Penot, and P. Le Quere, "Experimental and numerical investigation of turbulent natural convection in a large air-filled cavity," International Journal of Heat and Fluid Flow **25**, 824–832 (2004).

[52] A. Sergent, P. Joubert, S. Xin, and P. L. Quéré, "Resolving the stratification discrepancy of turbulent natural convection in differentially heated air-filled cavities Part II: End walls effects using large eddy simulation." International Journal of Heat and Fluid Flow **39**, 15–27 (2013).

[53] C. Cintolesi, A. Petronio, and V. Armenio, "Large eddy simulation of turbulent buoyant flow in a confined cavity with conjugate heat transfer," Physics of fluids **27**, 095109 (2015).

[54] J. Smagorinsky, "General circulation experiments with the primitive equations: I. The basic experiment," Monthly weather review **91**, 99–164 (1963).

[55] D. K. Lilly, "On the application of the eddy viscosity concept in the inertial sub-range of turbulence," NCAR manuscript **123** (1966).

[56] E. R. Van-Driest, "On turbulent flow near a wall," Journal of the aeronautical sciences **23**, 1007–1011 (1956).

[57] M. Germano, U. Piomelli, P. Moin, and W. H. Cabot, "A dynamic subgrid-scale eddy viscosity model," Physics of Fluids A: Fluid Dynamics **3**, 1760–1765 (1991).

[58] F. Nicoud and F. Ducros, "Subgrid-scale stress modelling based on the square of the velocity gradient tensor," Flow, turbulence and Combustion **62**, 183–200 (1999).

[59] D. Barhaghi and L. Davidson, "Natural convection boundary layer in a 5: 1 cavity," Physics of Fluids **19**, 125106 (2007).

[60] I. Celik, Z. Cehreli, and I. Yavuz, "Index of resolution quality for large eddy simulations," ASME Journal of Fluids Engineering **127**, 949–958 (2005).

[61] M. Klein, J. Meyers, and B. J. Geurts, "Assessment of LES quality measures using the error landscape approach," Quality and Reliability of Large-Eddy Simulations , 131–142 (2008).

[62] J. Patterson and J. Imberger, "Unsteady natural convection in a rectangular cavity," Journal of Fluid Mechanics **100**, 65–86 (1980).

[63] S. Thorpe, "On standing internal gravity waves of finite amplitude," Journal of Fluid Mechanics **32**, 489–528 (1968).

[64] J. S. Turner and J. S. Turner, *Buoyancy effects in fluids* (Cambridge university press, 1979).

[65] P. Le Quéré and M. Behnia, "From onset of unsteadiness to chaos in a differentially heated square cavity," Journal of fluid mechanics **359**, 81–107 (1998).

[66] F. Sebilleau, R. Issa, S. Lardeau, and S. Walker, "Direct numerical simulation of an air-filled differentially heated square cavity with Rayleigh numbers up to 10^{11}," Int. J. Heat Mass Tran. **123**, 297–319 (2018).

[67] P. Schlatter, Q. Li, G. Brethouwer, A. Johansson, and D. Henningson, "Simulations of spatially evolving turbulent boundary layers up to Re_θ = 4300," Int. J. Heat Fluid Fl. **31**, 251–261 (2010).

[68] P. Klebanoff, "Effect of free-stream turbulence on a laminar boundary layer," in *Bulletin of the American Physical Society*, Vol. 16 (1971) pp. 13–23.

[69] P. Durbin and X. Wu, "Transition beneath vortical disturbances," Annu. Rev. Fluid Mech. **39**, 107–128 (2007).

[70] R. Manceau, M. Wang, and D. Laurence, "Inhomogeneity and anisotropy effects on the redistribution term in Reynolds-averaged Navier-Stokes modelling," J. Fluid Mech. **438**, 307–338 (2001).

[71] R. Manceau and K. Hanjalić, "Elliptic Blending Model: A New Near-Wall Reynolds-Stress Turbulence Closure," Phys. Fluids **14**, 744–754 (2002).

[72] J. L. Lumley, "Computational Modeling of Turbulent Flows," in *Advances in Applied Mechanics*, Vol. 18 (Academic Press, New-York, 1978) pp. 123–175.

[73] S. Paolucci and D. R. Chenoweth, "Transition to chaos in a differentially heated vertical cavity," Journal of Fluid Mechanics **201**, 379–410 (1989).

[74] P. Le Quéré, "Accurate solutions to the square thermally driven cavity at high Rayleigh number," Computers & Fluids **20**, 29–41 (1991).

[75] R. Janssen and R. Henkes, "Influence of Prandtl number on instability mechanisms and transition in a differentially heated square cavity," Journal of Fluid Mechanics **290**, 319–344 (1995).

[76] P. G. Baines, S. J. Majumdar, and H. Mitsudera, "The mechanics of the Tollmien-Schlichting wave," Journal of fluid mechanics **312**, 107–124 (1996).

[77] Y. Jaluria and B. Gebhart, "On transition mechanisms in vertical natural convection flow," Journal of Fluid Mechanics **66**, 309–337 (1974).

[78] B. Gebhart and R. Mahajan, "Characteristic disturbance frequency in vertical natural convection flow," International Journal of Heat and Mass Transfer **18**, 1143–1148 (1975).

[79] B. Gebhart, "Transient response and disturbance growth in vertical buoyancy-driven flows," Journal of Heat Transfer **110**, 1166–1174 (1988).

[80] R. Dring and B. Gebhart, "A theoretical investigation of disturbance amplification in external laminar natural convection," Journal of Fluid Mechanics **34**, 551–564 (1968).

[81] Z. H. Qureshi and B. Gebhart, "Transition and transport in a buoyancy driven flow in water adjacent to a vertical uniform flux surface," International Journal of Heat and Mass Transfer **21**, 1467–1479 (1978).

[82] R. Mahajan and B. Gebhart, "An experimental determination of transition limits in a vertical natural convection flow adjacent to a surface," Journal of Fluid Mechanics **91**, 131–154 (1979).

[83] R. Henkes and C. Hoogendoorn, "On the stability of the natural convection flow in a square cavity heated from the side," Applied scientific research **47**, 195–220 (1990).

[84] M. Ravi, R. Henkes, and C. Hoogendoorn, "On the high-Rayleigh-number structure of steady laminar natural-convection flow in a square enclosure," Journal of Fluid Mechanics **262**, 325–351 (1994).

[85] A. F. Rius-Vidales and M. Kotsonis, "Unsteady interaction of crossflow instability with a forward-facing step," Journal of Fluid Mechanics **939**, A19 (2022).

[86] R. S. Downs and E. B. White, "Free-stream turbulence and the development of cross-flow disturbances," Journal of Fluid Mechanics **735**, 347–380 (2013).

[87] J. Serpieri and M. Kotsonis, "Three-dimensional organisation of primary and secondary crossflow instability," Journal of Fluid Mechanics **799**, 200–245 (2016).

[88] J. Serpieri, S. Y. Venkata, and M. Kotsonis, "Conditioning of cross-flow instability modes using dielectric barrier discharge plasma actuators," Journal of Fluid Mechanics **833**, 164–205 (2017).

[89] K. J. Groot, J. Serpieri, F. Pinna, and M. Kotsonis, "Secondary crossflow instability through global analysis of measured base flows," Journal of Fluid Mechanics **846**, 605–653 (2018).

[90] B. Gebhart, *Buoyancy-induced flows and transport* (Hemisphere Pub, 1988).

[91] A. M. Fraser and H. L. Swinney, "Independent coordinates for strange attractors from mutual information," Physical review A **33**, 1134 (1986).

[92] J. Feder, *Fractals* (Springer Science & Business Media, 2013).

[93] M. P. Juniper and R. I. Sujith, "Sensitivity and nonlinearity of thermoacoustic oscillations," Annual Review of Fluid Mechanics **50**, 661–689 (2018).

[94] L. Kabiraj, A. Saurabh, P. Wahi, and R. Sujith, "Route to chaos for combustion instability in ducted laminar premixed flames," Chaos: An Interdisciplinary Journal of Nonlinear Science **22**, 023129 (2012).

[95] R. Sujith and S. A. Pawar, *Thermoacoustic instability: A complex systems perspective* (Springer, 2021).

[96] Q. Zhou, H. Lu, B. Liu, and B. Zhong, "Measurements of heat transport by turbulent Rayleigh-Bénard convection in rectangular cells of widely varying aspect ratios," Science China Physics, Mechanics and Astronomy **56**, 989–994 (2013).

[97] M. Khaled, M. Ramadan, H. El-Hage, A. Elmarakbi, F. Harambat, and H. Peerhossaini, "Review of underhood aerothermal management: Towards vehicle simplified models," Appl. Therm. Eng. **73**, 842–858 (2014).

[98] J. Fang, D. Shaver, A. Tomboulides, M. Min, P. Fischer, Y.-H. Lan, R. Rahaman, P. Romano, S. Benhamadouche, Y. Hassan, A. Kraus, and E. Merzari, "Feasibility of full-core pin resolved CFD simulations of small modular reactor with momentum sources," Nucl. Eng. Des. **378**, 111143 (2021).

[99] B.-F. Wang, J.-L. Wu, J.-Z. Wu, K. L. Chong, Y.-L. Liu, and Q. Zhou, "Experimental study of heat transfer in a rectangular cell with built-in lattice channels," Phys. Fluids **35** (2023).

[100] S. M. S. Jameel, R. Manceau, and V. Herbert, "Sensitization of eddy-viscosity models to buoyancy effects for predicting natural convection flows," in *HEFAT 2019-14th International Conference on Heat Transfer, Fluid Mechanics and Thermodynamics* (2019).

[101] P. Bikkanahally, *Modelling turbulent flows in the natural convection regime using hybrid RANS-LES approaches*, Ph.D. thesis (2023).